Improving the global applicability of the RUSLE model – Adjustment of the topographical and rainfall erosivity factors

V. Naipal[1], C. Reick[1], J. Pongratz[1], K. Van Oost[2]

[1] {Max Planck Institute for Meteorology, Hamburg 20146, Germany}

[2] {Université catholique de Louvain, TECLIM – Georges Lemaître Centre for Earth and Climate Researh, Louvain-la-Neuve, Belgium}

Correspondence to: V. Naipal (victoria.naipal@mpimet.mpg.de)

Abstract

Large uncertainties exist in estimated rates and the extent of soil erosion by surface runoff on a global scale. This limits our understanding of the global impact that soil erosion might have on agriculture and climate. The Revised Universal Soil Loss Equation (RUSLE) model is due to its simple structure and empirical basis, a frequently used tool in estimating average annual soil erosion rates at regional to global scales. However, large spatial scale applications often rely on coarse data input, which is not compatible with the local scale on which the model is parameterized. Our study aims at providing the first steps in improving the global applicability of the RUSLE model in order to derive more accurate global soil erosion rates.

We adjusted the topographical and rainfall erosivity factors of the RUSLE model and compared the resulting erosion rates to extensive empirical databases from the USA and Europe. By scaling the slope according to the fractal method to adjust the topographical factor, we managed to improve the topographical detail in a coarse resolution global digital elevation model.

Applying the linear multiple regression method to adjust rainfall erosivity for various climate zones, resulted in values that compared well to high resolution erosivity data for different regions. However, this method needs to be extended to tropical climates, for which erosivity is biased due to the lack of high resolution erosivity data.

After applying the adjusted and the unadjusted versions of the RUSLE model on a global scale we find that the adjusted version shows a global higher mean erosion rate and more variability in the erosion rates. Comparison to empirical datasets of the USA and Europe shows that the adjusted RUSLE model is able to decrease the very high erosion rates in hilly regions that are observed in the unadjusted RUSLE model results. Although there are still some regional differences with the empirical databases, the results indicate that the methods used here seem to be a promising tool in improving the applicability of the RUSLE model on a coarse resolution on global scale.

1 Introduction

For the last centuries to millennia soil erosion by surface runoff is being accelerated globally due to human activities, such as deforestation and agricultural practices (Bork and Lang, 2003). Accelerated soil erosion is a process that triggers land degradation in the form of nutrient loss, a decrease in the effective root depth, water imbalance in the root zone and finally also productivity reduction (Yang *et al*., 2003). It is widely recognized that soil erosion has been a major threat to sustainable agriculture and food production across the globe since the start of agricultural activities (UNCCD, 2012, Walling, 2009). These effects of soil erosion are currently exacerbated by the global population growth and climatic changes. Organizations such as the United Nations Convention to Combat Desertification (UNCCD) try to address this problem by stating a new goal for Rio +20 of zero land degradation (UNCCD, 2012).

Another aspect underpinning the relevance of soil erosion on the global scale is the effect of erosion on global nutrient cycles. Recently, the biogeochemical components of Earth System Models (ESMs) became increasingly important in predicting the global future climate (Thornton *et al*., 2007, Goll *et al*., 2012). Not only the global carbon cycle but also other nutrient cycles such as the nitrogen and phosphorous cycles cannot be neglected in ESMs anymore (Goll *et al.*,2012, Gruber and Galloway, 2008, Reich *et al*., 2006). Soil erosion may have a significant impact on these biogeochemical cycles through lateral fluxes of sediment, but the impact on the global scale is still largely unknown. For example, Quinton *et al.* (2010) showed that erosion can significantly alter the nutrient and carbon cycling and result in lateral fluxes of nutrients that are similar in magnitude as fluxes induced by fertilizer application and crop removal. Regnier *et al.*

(2013) looked at the effect of human induced lateral fluxes of carbon from land to ocean and concluded that human perturbations, which include soil erosion, may have enhanced the carbon export from soils to inland waters.

In general, the effect of soil erosion on the global carbon cycle has received considerable attention after the pioneering work of Stallard (1998), who proposed that global soil erosion can result in sequestration of carbon by soils. After his work, the effect of soil erosion on the carbon cycle has been studied extensively, but there remains a large uncertainty in the effect of soil erosion on the carbon cycle. For example, several recent global assessments of the influence of soil erosion on the carbon cycle indicate a large uncertainty with a range from a source of 0.37 to 1 Pg C year^{-1} to a net uptake or sink of 0.56 to 1 Pg C year^{-1} (van Oost *et al*., 2007). Thus, in order to better constrain the global carbon budget and to identify optimal management strategies for land use, it is essential to have accurate estimates of soil erosion and its variability on a global scale.

Currently, there exists a large uncertainty in the global soil erosion rates as can be seen from recent studies that show rates between 20 and 200 Pg year^{-1} (Doetterl *et al*., 2012). This indicates that modelling soil erosion on a global scale is still a difficult task due to the very high spatial and temporal variability of soil erosion. Different approaches were previously applied to estimate soil erosion on a large or global scale. Most of these approaches are based on extrapolated data from agricultural plots, sediment yield or extrapolated river sediment estimates (Milliman and Syvitski, 1992, Stallard, 1998, Lal, 2003, Hooke, 2000, Pimentel *et al*.,1995, Wilkinson and McElroy, 2007).

An alternative approach is based on the use of soil erosion models, in order to be able to predict soil erosion rates for the past and future. One of the most applied models to estimate soil erosion on a large spatial scale is the semi-empirical/process-based Revised Universal Soil Loss Equation (RUSLE) model (Renard *et al*., 1997). This model stems from the original Universal Soil Loss Equation (USLE) model developed by USDA (USA Department of Agriculture), which is based on a large set of experiments on soil loss due to water erosion from agricultural plots in the United States (USA). These experiments covered a large variety of agricultural practices, soil types and climatic conditions, making it a potentially suitable tool on a regional to global scale. The RUSLE model predicts the average annual soil erosion rates by rainfall and is formulated as a product of a rainfall erosivity factor (*R*), a slope steepness factor (*S*), a slope length factor (*L*), a soil erodibility factor (*K*), a land cover factor (*C*) and a support practice factor (*P*). The RUSLE model was first applied on a global scale by Yang *et al*. (2003) and Ito (2007) for estimating the global soil erosion potential. Various limitations were observed when applying this model on global scale. Firstly, the model is originally developed to be applicable on the agricultural plot scale. This makes the model incompatible with the coarse spatial scale of global datasets on soil erosion influencing factors such as precipitation, elevation, land-use and soil characteristics. Secondly, the RUSLE and USLE models were parameterized for environmental conditions of the United States (USA), and are thus not directly applicable to other areas in the world. Thirdly, only sheet and rill erosion are considered. Finally, the RUSLE model does not contain sediment deposition and sediment transport terms, which are closely linked to soil erosion.

However, the RUSLE model is to our knowledge one of the few erosion models that has the potential to be applied on a global scale due to its simple structure and empirical basis. Therefore, it is of key importance to address the above mentioned limitations first.

To address the first two limitations, Van Oost *et al*. (2007) presented in their work a modified version of the USLE model for application on agricultural areas on global scale. They based their model on large-scale experimental soil erosion data from the USA (National Resource Inventory, NRI database, USDA, 2000) and Europe, by deriving reference factors for soil erosion on agricultural land, and for certain USLE parameters. They also introduced a procedure to scale slope, which is an important parameter in the topographical factors *S* and *L* of the USLE/RUSLE model. In this scaling procedure slope was scaled from the GTOPO30 1km resolution digital elevation model (USGS, 1996) to the coarser resolution of the erosion model. This method was based on high resolution OS Ordnance (10 m resolution) and SRTM data on elevation (90 m resolution, International Centre for Tropical Agriculture, CIAT) for England and Wales.

Doetterl *et al*. (2012) showed that together with the *S* factor, the rainfall erosivity or *R* factor explain up to 75 % of the erosion variability across agricultural areas at the large watershed scale. These factors represent the triggers for soil erosion by providing energy for soil to erode. They can also be seen as the natural components of the RUSLE model, as they include very little or no modification by human activities (Angulo-Martínez *et al*., 2009) apart from indirect effects on precipitation and extreme events due to anthropogenic climate change. In this way they represent the natural environmental constraints to soil erosion that are important to capture before the effect of human activities on soil erosion through land use change can be investigated.

Previous studies on global soil erosion calculated the global *R* factor based on the total annual precipitation (Renard and Freimund, 1994). This method is different from the method presented in the original RUSLE model (Renard *et al*., 1997), which is mainly based on 30 minute precipitation intensity. The reason for the method of Renard and Freimund is the lack of high resolution precipitation intensity on a global scale. However, high resolution precipitation intensity is an important explaining parameter of the *R* factor and therefore, the applicability of the method of Renard and Freimund is limited.

The overall objective of our study is to extend the applicability of the RUSLE model to a coarse resolution at global scale, in order to make the model compatible with ESMs. This would enable future studies on the effects of soil erosion for the past, current and future climate. To this end, we develop generally applicable methods that improve the estimation of slope and climatic factors from coarse resolution global datasets. These methods should not only be applicable across agricultural areas as in the studies of Van Oost *et al*. (2007) and Doetterl *et al*. (2012), but also across non-agricultural areas. We adjust the *S* factor to the coarse resolution of the global scale based on the scaling of slope according to the fractal method. The adjustment of the *R* factor to the global scale is based on globally applicable regression equations. We derived these regression equations for different climate zones based on parameters for precipitation, elevation and the simple precipitation intensity. This approach is validated using several high resolution datasets on the *R* factor. Finally, the effects of these adjustments of both factors on global soil erosion rates are investigated separately and tested against independent estimates of soil erosion from high resolution and high precision datasets of Europe and the USA.

2. Adjustment of the topographical factor

2.1 Scaling slope according to the fractal method

The topographical factors of RUSLE are the slope steepness factor (*S*) and a slope length factor (*L*). The S factor is generally computed by the continuous function of Nearing (1997):

$$S=1.5+\frac{17}{1+e^{(2.3-6.1*\sin\theta)}} \quad (1)$$

And the L factor is computed according to Renard *et al*. (1997):

$$L=\left(\frac{l}{22.13}\right)^{m} \quad (2)$$

where: $m=\frac{F}{1+F}$ and $F=\frac{(\sin\theta/0.0896)}{(3*(\sin\theta)^{0.8}+0.56)}$ (3)

in which θ is the slope and l is the slope length in meters.

As seen in the equations 1 to 3, slope is a crucial parameter and thus an accurate estimation is essential in deriving accurate estimates of the L and S factors and soil erosion rates. For an accurate estimation of the slope, input elevation data from digital elevation models (DEMs) should capture the detailed spatial variability in elevation. However, global DEMs are often too coarse to capture the detailed topography because of the surface smoothening effect. To account for this problem it is assumed that topography is fractal. Following Klinkenberg and Goodchild (1992) and Zhang *et al*. (1999), slope can be expressed as a function of the spatial scale by applying the variogram equation. The variogram equation is used to approximate the fractal dimension of topography and is expressed as follows:

$$(Z_p-Z_q)^2=k\, d_{pq}^{4-2D} \quad (4)$$

so that:

$$\frac{|Z_p-Z_q|}{d_{pq}}=\alpha\, d_{pq}^{1-D} \quad (5)$$

where Z_p and Z_q are the elevations at points p and q, d_{pq} is the distance between p and q, k is a constant, $\alpha = k^{0.5}$, and D is the fractal dimension. Because the left side of Eq. (5) represents the slope, it can be assumed that the slope (θ) is related to the spatial scale or the grid size (d) in:

$$\theta= \alpha\, d^{1-D} \quad (6)$$

This result implies that by calculating the fractal properties (D and α) Eq. (6) can be used to calculate slope at any specified d. The local fractal dimension (D) describes the roughness of the topography while the local value of α is related to the concept of lacunarity, which is a measure of the size of “gaps” (valleys and plains) in the topography (Zhang *et al.*, 2002). To estimate the spatial variations of D and α, Zhang *et al*. (1999) proposed to relate these parameters to the standard deviation of elevation. Hereby it is assumed that the standard deviation of elevation does not change much with the DEM resolution. D is then calculated as a function of the standard deviation (σ) in a 3 x 3 pixels moving window, as proposed by Zhang *et al*. (1999):

$$D=1.13589+0.08452\ln\sigma \quad (7)$$

To estimate α we used the modified approach by Pradhan *et al*. (2006). They derived α directly from the steepest slope in a 3 x 3 pixels moving window, called $\alpha_{steepest}$ in the following. Having obtained $\alpha_{steepest}$ and D from a grid at a given resolution, the scaled slope (θ_{scaled}) for a target grid resolution (d_{scaled}) is obtained by:

$$\theta_{scaled}=\alpha_{steepest}\, d_{scaled}^{1-D} \quad (8)$$

Pradhan *et al.* (2006) also showed that in their case study the ideal target resolution for downscaling slope was 150 m. This is due to the breakdown of the unifractal concept at very fine scales, which was shown to happen at a scale of 50 m. Altogether, this fractal method shows that a high resolution slope can be obtained from a low resolution DEM as is needed by the RUSLE model.

2.2 Application of the fractal method on global scale

In this study, we investigate the performance of the fractal method on a global scale using different global DEMs as a starting point. The target resolution of downscaling is put to 150 m (about 5 arc-second) according to Pradhan *et al*. (2006). It should be noted that the spatial scale on which the original RUSLE and USLE models are operating, is usually between 10 and 100 m, which indicates that the 150 m target resolution may be still too coarse for a correct representation of slope. The DEMs that are used here are given in Table 1.

As reported in previous studies (Zhang *et al.*, 1999, Chang and Tsai, 1991, Zhang and Montgomery, 1994), the average slope decreases with decreasing DEM resolution. This confirms the expectation of loss of detail in topography at lower DEM resolutions. A large difference is found between the unscaled global average slope from the 5 arc-minute and the 30 arc-second DEMs, which is in the order of 0.017 m m^{-1} or 74 % (Table 2). After applying the fractal method, the scaled slopes at 150 m target resolution from all DEMs all increased significantly compared to the unscaled slopes (Fig. 1). However, there is still a difference of about 0.05 m m^{-1} or 8.5 % between the scaled slopes from the 5 arc-minute and the 30 arc-second DEMs (Table 2). This difference can be attributed to several factors. One factor could be the underlying assumption that the standard deviation of elevation (σ) is independent of the DEM resolution. Although σ does not change much when considering different resolutions, there is still a general decrease in mean global σ when going from the 5 arc-minute to the 30 arc-second DEM (Table 2). Due to the dependence of the fractal dimension (D) on σ (Zhang *et al.*, 1999), a decrease of σ leads to a decrease in D and therefore an increase in the scaled slope. Other factors that could play a role here are the dependence of $\alpha_{steepest}$ on the steepest slope, and the breakdown of the fractal method at certain scales and in certain environments. Zhang *et al.* (1999) mentioned that the scaling properties of slope are affected in very coarse resolution DEMs if σ changes considerably. On the other hand, Pradhan *et al*. (2006) mentioned the breakdown of the fractal method at very fine scales. This can indicate that the 150 m target resolution is not appropriate for some topographically complex regions in the world or, as addressed by Zhang *et al*. (1999), the DEMs used in this study are too coarse to scale down the slope to 150 m accurately for these regions.

After applying the fractal method on a 30 arc-second resolution DEM, the scaled slope shows a clear increase in detail, while the unscaled slope shows a strong smoothening effect (Fig. 2A and 2B). It is found that after scaling the slope values range from 0 to 85 degrees and are less than 2 degrees in 80 % of the area. In contrast, all slope values are less than 45 degrees and range between 0 and 2 degrees in 89 % of this area when slope is computed directly from the 30 arc-second DEM.

The scaled slope from the 30 arc-second DEM will be used in this study to estimate the global soil erosion rates by the RUSLE model.

3. Adjustment of the rainfall erosivity factor

3.1 The approach by Renard and Freimund (1994)

Rainfall erosivity (R factor) is described by Hudson (1971) and Wischmeier and Smith (1978) as the result of the transfer of kinetic energy of raindrops to the soil surface. This causes a detachment of soil and the downslope transport of the soil particles, depending on the amount of energy, rainfall intensity, soil type and cover, topography and management (Da Silva, 2004). The original method of calculating erosivity is described by Wischmeier and Smith (1978) and Renard *et al.* (1997) as:

$$R= \frac{1}{n} * \sum_{j=1}^{n} \sum_{k=1}^{m_j} (EI_{30})_k \qquad (9)$$

where n is the number of years of records, m_j is the number of storms of a given year j, and EI_{30} is the rainfall erosivity index of a storm k. The event's rainfall erosivity index EI_{30} (MJ mm ha^{-1} hour^{-1}) is defined as:

$$EI_{30}=I_{30} * \sum_{r=1}^{m} e_r v_r \qquad (10)$$

where e_r and v_r are, respectively, the unit rainfall energy (MJ ha^{-1} mm^{-1}) and the rainfall depth (mm) during a time period r, and I_{30} is the maximum rainfall intensity during a time period of 30 minutes (mm hour^{-1}). The unit rainfall energy, e_r, is calculated for each time period as:

$$e_r=0.29*(1-0.72*e^{-0.05*i_r}) \qquad (11)$$

where i_r is the rainfall intensity during the time period (mm hour^{-1}).

The information needed to calculate the R factor according to the method of Wischmeier and Smith (1978) is difficult to obtain on a large spatial scale or in remote areas. Therefore, different studies have been done on deriving regression equations for the R factor (Angulo-Martinez *et al.*, 2009, Meusburger *et al.*, 2012, Goovaerts, 1999, Diodato and Bellocchi, 2010). Most of these studies, however, concentrate on a specific area and can therefore not be implemented on the global scale. Studies on global soil erosion estimation by the RUSLE model or a modified version of it (Doetterl *et al.*, 2012, van Oost *et al.*, 2007, Montgomery, 2007, Yang *et al.*, 2003) have all used the method of Renard and Freimund (1994). Renard and Freimund related the R factor to the total annual precipitation based on erosivity data available for 155 stations in the USA, shown in the following equations:

$$R=0.0483*P^{1.61}, \qquad P <= 850 \text{ mm}$$

$$R=587.8-1.219*P+0.004105*P^2, \qquad P > 850 \text{ mm} \qquad (12)$$

To test how this method performs globally, we calculated the *R* factor according to the method of Renard and Freimund (Eq. 12) first. Here we used the 0.25 degree resolution annual precipitation data from the Global Precipitation Climatology Center (GPCC) product (Table 1). Then, we selected three regions to validate the resulting *R* values and their variability: the USA (EPA, 2001), Switzerland (Meusburger *et al.*, 2011), and the Ebro basin in Spain (Angulo-Martinez *et al.*, 2009). For these regions high resolution erosivity data are available obtained from pluviographic data from local meteorological stations across the whole region.

Figure 3 shows that the *R* values computed with the Renard and Freimund method strongly overestimate *R* when compared to the high resolution *R* data of the selected regions. For the USA the *R* factor of Renard and Freimund shows an overall overestimation for western USA and for a large part of eastern USA when compared to the high resolution *R* (Table 7 and Fig. 3A). Especially a strong overestimation is seen for the north-west coast of the USA. This region is known to have complex rainfall patterns due to the presence of mountains and high local precipitation intensities with frequent snow fall (Cooper, 2011). It should be noted that the USA is not a completely suited case study for testing the *R* values computed with the Renard and Freimund method, as this method is based on climate data from stations in the USA. The available high resolution or observed data on the *R* factor from Switzerland and the Ebro basin are better suited for an independent validation.

For Switzerland, which has a complex precipitation variability influenced by the relief of the Alps (Meusburger *et al.*, 2012), the *R* factor of Renard and Freimund shows a strong overall overestimation when compared to the high resolution *R* values (Table 7 and Fig. 3B). For the Ebro basin located in Spain, the observed *R* data were available for the period 1997-2006 from Angulo-Martinez *et al.*, 2009. Also here the method of Renard and Freimund overestimates the *R* factor and is not able to reproduce the high spatial variability of the *R* data (Table 7 and Fig. 3C).

3.2 The linear multiple regression approach using environmental factors

To better represent the *R* factor on a global scale, the *R* estimation was based on the updated Köppen-Geiger climate classification (Table 3 and Fig. 4). The Köppen-Geiger climate classification is a global climate classification and is based on the vegetation distribution connected to annual cycles of precipitation and temperature (Lohmann *et al.*, 1993). The reason for this approach is that this classification system includes annual cycles of precipitation and is thus indirectly related to precipitation intensity. Based on this, it is possible to derive regression equations for the *R* factor that are applicable for each individual climate zone of the classification. This provides a basis to calculate the *R* factor with coarse resolution data on a global scale.

As a basis for deriving the regression equations for the *R* factor we used high resolution *R* maps of the USA from EPA (2001). The USA covers most of the world's climate zones and is also the largest region with available high resolution *R* data. Linear multiple regression was used to adjust *R*:

$$\log(R_i)=\beta_0+\sum_{j=1}^{n}\beta_{i_j} * \log(X_{i_j}) +\varepsilon_i, \text{ for } i = 1, 2, \ldots, n \quad (13)$$

where X is the independent explanatory variable, j is the number of explanatory variables, β is a constant and ε is the residual.

The regression operates on one or more of the following parameters (X_j): total annual precipitation (GPCC 0.25 degree product), mean elevation (ETOPO 5 DEM), and the simple precipitation intensity index, SDII. It should be mentioned that the SDII was only available on a very coarse resolution of 2.5 degree resolution for certain regions on earth, such as parts of Europe and the USA. The SDII is calculated as the daily precipitation amount on wet days (>= 1 mm) in a certain time period divided by the number of wet days in that period. Previous studies that performed regression of *R* showed that precipitation and elevation were in most cases the only explanatory variables (Meusburger *et al*., 2012, Mikhailova *et al*., 1997, Goovaerts, 1999, Diodato and Bellocchi, 2010, Angulo-Martinez *et al*., 2009). Here, we added to the regression the SDII as it is a simple representation of precipitation intensity, which is an important explaining variable of the *R* factor. The precipitation and SDII datasets were rescaled to a 5 arc-minute resolution (corresponding to 0.0833 degree resolution) to match the Köppen-Geiger climate classification data that was available at the resolution of 6 arc-minute (corresponding to 0.1 degree).

Furthermore, high resolution erosivity data from Switzerland (Meusburger *et al*., 2011) and annual precipitation from the GPCC 0.5 degree product were used to derive the regression equations for the *R* factor for the polar (E) climate zones. These climate zones are not present in the USA. For the rest of the climate zones that are not present in the USA it was difficult to obtain high resolution erosivity data. Therefore, we maintained the method of Renard and Freimund for those climate zones to calculate erosivity. Also, we kept the *R* factor of the Renard and Freimund method if no clear improvement of the *R* factor was found when using the new regression equations for a specific climate zone. Here, we mainly used the r^2 combined with the residual standard error to evaluate if the new regression equations showed a clear improvement in the *R* factor. The Renard and Freimund *R* factors where kept for the hot arid climate zone (BWh) and the temperate climate zone with a hot summer (Csa) in the USA. These are just two climate zones out of the 17 evaluated ones, which show that the Renard and Freimun method performs as good as or slightly better than the regression method. All datasets for deriving the *R* factor are described in Table 1.

3.3 Application of the linear multiple regression method on a global scale

Tables 4 and 5 show the resulting regression equations for climate zones for which we found initially a low correlation between the *R* values calculated by the method of Renard and Freimund and the high resolution *R* values from EPA (2001) and Meusburger *et al*. (2011). Figure 5 shows for each addressed climate zone how the method of Renard and Freimund and the new regression equations compare to the high resolution *R* of the USA. For the cold climate zones with a dry summer (Ds) the new regression equations show only a slight improvement as compared to the method of Renard and Freimund. Also for the polar climate zones (E) the new regression equations still show a significant bias. However, they perform much better compared to the method of Renard and Freimund. For most of the addressed climate zones the simple precipitation intensity index (SDII) explains a large part of the variability in the *R* factor. The elevation plays a smaller role here. Elevation can be an important explaining variable in regions with a high elevation variability, which then affects the precipitation intensity.

From Table 4 and Table 6 it can be concluded that the *R* factor in climate zones without a dry season (f), can be easily explained by the total annual precipitation and the SDII. Dry climate zones, especially dry summer climate zones showed a weaker correlation. This is most probably due to the fact that the SDII is too coarse to explain the variability in the low precipitation intensity in the summer. It is also interesting to see that even though the SDII was derived from a very coarse resolution dataset, it turned out to be still important for deriving more accurate *R* values.

We also show for each addressed climate zone a comparison of the newly computed average *R* factor with the average high resolution *R* factor, and the uncertainty range (Table 6). The uncertainty range was computed by taking into account the standard deviation of each of the parameters in the regression equations. As mentioned before, the polar climate zones (E) showed the largest uncertainty range. The new regression equations significantly improved the *R* values and spatial variability in the western USA, and lead to an average *R* factor that was closer to the data mean (Table 7 and Fig. 6A). Although the new regression equations show a bias for the polar climate zones (E) (the minimum and maximum *R* values are not captured), the resulting mean *R* values for Switzerland show a strong improvement (Table 7 and Fig. 6B).

Furthermore, the variability in the estimated *R* factor compares well with the variability of the high resolution *R* factor. It should be noted that Switzerland is not an independent case study for the polar climate zones (E), as the high resolution *R* values from this case study were used in our regression analysis. However, the Ebro basin case study confirms the strong improvement for the polar climate zones (E) (Fig. 6C). As the high resolution *R* values of the USA and Switzerland were used to derive the regression equations, the third case study, the Ebro basin in Spain, provided an important independent validation. For the Ebro basin, the new regression equations not only improve the overall mean but also capture the minimum *R* values better. This resulted in an improved representation of the *R* variability (Table 7 and Fig. 6C). In Fig. 6C, however, there is a clear pattern separation in the newly computed *R* values, which is due to the fact that the SDII data are not available for part of the Ebro basin. As mentioned before, SDII is an important explaining parameter in the regression equations for most of the addressed climate zones.

Figure 7A shows the global patterns of the estimated *R* factor from the method of Renard and Freimund and the new regression equations. Figure 7B shows a difference plot between the estimated *R* factor with the method of Renard and Freimund and the *R* factor estimated with the new regression equations. The new regression equations significantly reduced the *R* values in most regions. However, the tropical regions still show unrealistic high *R* values (maximum *R* values go up to $1 * 10^5$ MJ mm ha^{-1} h^{-1} $year^{-1}$). This is because the *R* factor was not adjusted for the tropical climate zones due to the lack of high resolution *R* data. Oliveira *et al*. (2013) found for the *R* factor in Brazil that the maximum *R* values for the tropical climate zones reach 22,452 MJ mm ha^{-1} h^{-1} $year^{-1}$. We find *R* values in Brazil that exceed this maximum *R* value found by Oliveira *et al*. (2013).

Finally, it should be noted that the purpose of the adjusting methods for the *S* and *R* factors in this study is to capture more accurately the large scale mean erosion rates rather than the extremes. Therefore, even though the new regression equations are still not accurate enough for certain climate zones, it is important that the average *R* factor is represented well. The approach for adjusting the *R* factor also showed that although there is no high temporal resolution precipitation intensity data available on a global scale, the *R* factor can still be represented well for most climate zones on a large spatial scale. This can be done by using other parameters, such as elevation, and especially a representative of precipitation intensity, such as the SDII. The SDII played an important role here as it improved the estimation of the *R* factor significantly, even though data was only available at a very low resolution as compared to the other datasets of precipitation, elevation and climate zone classification.

4 Global application of the adjusted RUSLE model

4.1 Computation of the soil erodibility and land cover factors

In the following we demonstrate the consequences of the new parameterizations of the *S* and *R* factors for global soil erosion rates. First, we compute the other individual RUSLE factors, soil erodibility (*K*) and crop cover (*C*). Estimations of the *K* factor we based on soil data from the gridded 30 arc-second Global Soil Dataset for use in Earth System Models (GSCE). GSCE is based on the Harmonized World Soil database (HWSD) and various other regional and national soil databases (Shangguan *et al*., 2014). We used the method of Torri *et al.* (1997) to estimate the *K* factor, and gave volcanic soils a *K* factor of 0.08 t ha h ha^{-1} MJ^{-1} mm^{-1}. This because these soil types are usually very vulnerable to soil erosion, and the observed *K* values are beyond the range predicted by the method of Torri *et al*. (1997) (van der Knijff *et al*., 1999). To account for the effect of stoniness on soil erosion we used a combination of the methods by Cerdan *et al*. (2010) and Doetterl *et al*. (2012), who based their methods on the original method of Poesen *et al*. (1994). For non-agricultural areas we used the method of Cerdan *et al*. (2010), where they reduced the total erosion by 30 % for areas with a gravel percentage larger or equal to 30 %. For agricultural and grassland areas we used the method of Doetterl *et al*. (2012), where erosion was reduced by 80 % in areas where the gravel percentage exceeded 12 %.

We calculated the *C* factor according to the method of De Jong *et al*. (1998), using 0.25 degree Normalized Difference Vegetation Index (NDVI) and land use data for the year 2002. An important limitation of this method is the fact that in winter the *C* factor is estimated too high (van der Knijff *et al*., 1999). This is because the method does not include the effects of mulch, decaying biomass and other surface cover reducing soil erosion. To prevent the *C* factor of being too high, maximum *C* values for forest and grassland of 0.01 and 0.05 for pasture were used. Doetterl *et al*. (2012) showed that the slope length (*L*) and support practice (*P*) factors do not contribute significantly to the variation in soil erosion at the continental scale to global scale, when compared to the contribution of the other RUSLE factors (S, R and C). However, this does not mean that their influence on erosion should be ignored completely. They may play an important role in local variation of erosion rates. In our erosion calculations we do not include these factors, because we have too little or no data on these factors on a global scale. Including them in the calculations would only add an additional large uncertainty to the erosion rates. This would make it more difficult to judge the improvements we made to the *S* and *R* factors.

4.2 Computation of global soil erosion rates and comparison to empirical databases

We applied the RUSLE model with the settings mentioned in the previous paragraph on a 5 arc-minute resolution on global scale for the present time period (see time resolutions of datasets in Table 1). We calculated global soil erosion rates with four different versions of the RUSLE model: (a) the unadjusted RUSLE, (b) RUSLE with only an adjusted *S* factor, (c) RUSLE with only an adjusted *R* factor and (d) the adjusted RUSLE (all adjustments included).

We found a global average soil erosion rate for the adjusted RUSLE of 6.5 t ha^{-1} $year^{-1}$ (Fig. 8A). When including the uncertainty arising from applying the linear multiple regression method, the mean global soil erosion rate differs between 5.3 and 15 t ha^{-1} $year^{-1}$. Furthermore, the RUSLE version with only an adjusted *S* factor shows the highest average global soil erosion rate, while the lowest rate is found for the RUSLE version with only the adjusted *R* factor (Table 8). Figure 8C shows the difference between the erosion rates of the S adjusted RUSLE and the unadjusted

RUSLE versions. The erosion rates are in general increased here, and mostly pronounced in mountainous regions. This feature is 'dampened' when adjusting the R factor. The difference between the R adjusted RUSLE and unadjusted RUSLE versions (Fig. 8D) shows that the erosion rates are overall decreased in regions where the adjustments are made. When combining both adjustments of the RUSLE model in the fully adjusted RUSLE version and subtract the unadjusted RUSLE erosion rates (Fig. 8B), erosion rates are slightly decreased in areas where the R factor is adjusted. However, for the tropics there an increase in erosion rates is found in the fully adjusted RUSLE due to the lack of adjusting the R factor there. This indicates that these two factors balance each other, and that it is important to have a correct representation of all the RUSLE factors on a global scale in order to predict reliable erosion rates.

In this study the *K* and *C* factors are not tested and adjusted for a coarse resolution at global scale and thus validation with existing empirical databases on soil erosion is not fully justified. However, to test if the global erosion rates are in an acceptable range, they are compared to erosion estimates from the NRI database for the USA, and erosion estimates from the study of Cerdan *et al*. (2010) for Europe. These are to our knowledge the only large scale high resolution empirical databases on soil erosion.

The NRI database contains USLE erosion estimates for the year 1997, which are available at the Hydrologic Unit 4^{th} Code (HUC4) watershed level. We aggregated the resulting erosion rates from the adjusted and unadjusted RUSLE models to the HUC4 watershed level. The results show that the average erosion rates from the adjusted RUSLE model come closer to that of the NRI database (Table 9 and Fig. 9A). However, the maximum average HUC4 soil erosion rate from the adjusted RUSLE is somewhat higher compared to the NRI database. From these results we can conclude that the erosion rates of the adjusted RUSLE fall in the range of observed values, but that there are still some local overestimations. Some of these overestimations can be found in south west of the USA where the adjusted RUSLE shows a slightly worse performance compared to the unadjusted RUSLE. The *R* factor in this region was not changed as it was already estimated well by the method of Renard and Freimund, however, the *S* factor increased due to the hilly terrain. Without adjusting the other RUSLE factors (*K* and *C*), this resulted in an overall increase in soil erosion rates. This indicates that the other RUSLE factors may play an important role in this region. Furthermore, we see that along the west coast of the USA the erosion values are not much improved with the adjusted RUSLE model. This is mainly because some climate zones such as the temperate climate zone with a dry and warm summer (Csb) prevail in this region, for which the *R* factor is still difficult to estimate in a correct way (Table 4).

For Europe, Cerdan *et al.* (2010) used an extensive database of measured erosion rates on plots under natural rainfall. They extrapolated measured erosion rates to whole Europe (European Union area) and adjusted them with a topographic correction. This correction was based on the *L* and *S* factors of the RUSLE model. They also applied a correction to account for soil stoniness. For comparison, the soil erosion rates from Cerdan *et al.* (2010) and the RUSLE estimates in our study are aggregated at country level. The performance of the adjusted RUSLE model was not as good for Europe as compared to the USA. This is not surprising as the RUSLE model is based on soil erosion data of the USA. However, also on the European scale the adjusted RUSLE model performed better than the unadjusted RUSLE model (Table 9 and Fig. 9B). Especially the large erosion rates in the south of Europe as observed in the results of the unadjusted RUSLE model are less extreme in the adjusted RUSLE model. Still, the overall average erosion rate for Europe is overestimated by approximately two times (Table 9).

The biases in erosion rates as seen for the south west of the USA and south Europe can be attributed to several factors. As mentioned before, the other RUSLE factors (*K* and *C*) and the way they interact with the *R* and *S* factors are not adjusted to the coarse resolution at global scale. We found no clear signal for which land cover types the adjusted RUSLE performs better or worse. In general, we can see that the adjusted RUSLE model still overestimates erosion rates for most land cover types. A short analysis for Europe showed that the largest biases are found for shrubs, and the least for grassland. However, a more explicit analysis is needed to find out how we can improve the contribution of land cover and land use to erosion rates in the RUSLE model. Explicitly including the interaction between the *C* and *R* factor on a monthly timescale could be crucial. This is very important for example in areas with agriculture, and areas with a strong seasonal character. Another aspect related to improving the *C* factor is looking at the location of land use in a certain grid cell. If the land use in a grid cell is located on steep slopes the resulting erosion in that grid cell would be higher than when it would be located in the flatter areas. In this study, however, only mean fractions of land cover and the NDVI are used for each grid cell. This can lead to possible biases in the resulting erosion rates.

Furthermore, land management is not accounted for in this study, which could introduce an important systematic bias in the soil erosion rates for especially agricultural areas. Land management is represented by the *P* factor in the original USLE, however, it is partly also incorporated in the *C* factor for agricultural land use through plant residues, cover crops and tillage. A limitation of the NDVI approach to estimate the *C* factor lies therefore in the inability to estimate this land management effect. Applying this method also limits the interaction between the *R* and *C* factors on a monthly to seasonally scale, because this interaction is partly based on land management.

Furthermore, uncertainties in the coarse resolution land cover/land use, soil and precipitation datasets that are not accounted for, can lead to the model biases. Also, better adjustment of the *R* factor for climate zones such as the polar climates (E) could help improving the overall results. Some biases in the erosion rates can also be attributed to the fact that stepped relief, where flat plateaus are separated by steep slopes, are not well captured by the 150 m target resolution used in the fractal method to scale slope. In this way erosion would be overestimated in these areas. Finally, errors and limitations in the observational datasets can also contribute to the differences between model and observations. The study of Cerdan *et al.* (2010) on Europe for example, used extrapolation of local erosion data to larger areas that could introduce some biases. Also, the underlying studies on measured erosion rates used different erosion measuring techniques that can be linked to different observational errors.

5 Conclusions

In this study we introduced specific methods to adjust the topographical and rainfall erosivity factors to improve the application of the RUSLE model on global scale, using coarse resolution input data.

Our results show that the fractal method by Zhang *et al.* (1999) and Pradhan *et al.* (2006) can be applied on coarse resolution DEMs to improve the resulting slope. Although the slope representation improved after applying this method, the results still show a slight dependence on the original grid resolution. This is attributable to several factors such as the underlying assumption that the standard deviation of elevation (σ) is independent of the DEM resolution, and to the breakdown of the fractal method at certain scales.

We compared the rainfall erosivity calculated by the method of Renard and Freimund to available high resolution or observed erosivity data of the USA, Switzerland and the Ebro basin. We find that this method results in overall significant biases in erosivity. Therefore, we implemented a linear multiple regression method to adjust erosivity for climate zones of the Köppen-Geiger climate classification system in the USA. Using precipitation, elevation and the simple precipitation intensity index as explaining parameters, the resulting adjusted erosivity compares much better to the observed erosivity data for the USA, Switzerland and the Ebro basin. Not only the mean values but also the spatial variability in erosivity is improved. It was surprising to notice that using the rather coarse resolution simple precipitation intensity index in the regression analysis made it possible to explain much of the variability in erosivity. This, once more, underpins the importance of precipitation intensity in erosivity estimation.

After calculating the newly adjusted erosivity on global scale, it is apparent that the tropical climate zones, for which erosivity was not adjusted, show strong overestimations in some areas. This shows that adjusting erosivity for the tropical climate zones should be the next step. The challenge is to find enough reliable long term and high resolution erosivity data for those regions.

To investigate how the adjusted topographical and rainfall erosivity factors affect the global soil erosion rates, we applied the adjusted RUSLE model on global scale. We found an average global soil erosion rate of 6.5 t ha^{-1} year^{-1}. It is, however, difficult to provide accurate uncertainty estimates to these global erosion rates, and to provide a good validation with observations. This is due to lack of high resolution data on other individual RUSLE factors such as the land cover, soil erodibility, slope length and support practice. These RUSLE factors are therefore not adjusted for application on a coarse resolution on global scale. We argue that it is important to focus on adjusting the other RUSLE factors, for an improved application of the RUSLE model on global scale. The next step would be to better capture the anthropogenic contribution to global soil erosion. This can be done by adjusting first of all the land cover factor to a coarse resolution application, and focus on the interaction of this factor with rainfall erosivity on a monthly to seasonal basis. This is important, because the land cover factor has strong interactions with the rainfall erosivity factor, and includes the effect of human activities on erosion through agricultural activities and land management.

To test if the soil erosion rates from the adjusted RUSLE model are in a realistic range, we compared the results to the USLE erosion estimates for the USA from the NRI database, and the erosion estimates for Europe from the study of Cerdan *et al.* (2010). The adjusted RUSLE soil erosion rates, which we aggregated to the watershed level, show a better comparison with the NRI USLE estimates than the unadjusted RUSLE erosion rates. For Europe the comparison of the adjusted RUSLE soil erosion rates to the study of Cerdan *et al.* (2010) were not as good as for the USA. This is not surprising due to the fact that the parameterizations of the RUSLE model are based on soil erosion data of the USA. However, also for Europe, the adjusted RUSLE model performs better than the unadjusted RUSLE model.

We find overestimations by the adjusted RUSLE model for hilly regions along the west coast of the USA, and for south of Europe. We argue that besides for reasons mentioned before, these biases are due to the fact that the topographical detail may not be enough in some regions to capture the true variability in soil erosion effects by topography. Also, erosivity could not be adjusted for some climate zones that are not present in the USA or Switzerland, and needs to be further improved for climate zones such as the polar climate zones.

We conclude that even though there is still much improvement of the RUSLE model possible with respect to topography and erosivity, the methods proposed in this study seem to be promising tools for improving the global applicability of the model. A globally applicable version of the RUSLE model, together with data on environmental factors from Earth System Models (ESMs), can provide the possibility for future studies to estimate accurate soil erosion rates for the past, current and future time periods.

Acknowledgements

We like to thank the anonymous reviewers for their useful comments. The article processing 554 charges for this open-access publication have been covered by the Max Planck Society. J. Pongratz was supported by the German Research Foundation's Emmy Noether Program (PO 1751/1-1).

References

1 Amante, C. and Eakins, B. W.: ETOPO1 1 Arc-Minute Global Relief Model: Procedures, Data Sources and Analysis, NOAA Technical Memorandum NESDIS NGDC-24, National Geophysical Data Center, NOAA, 2009.

2 Angulo-Martínez, M., López-Vicente, M., Vicente-Serrano, S. M. and Beguería, S.: Mapping rainfall erosivity at a regional scale: a comparison of interpolation methods in the Ebro Basin (NE Spain), J. Hydrol. Earth Syst. Sc., 13, 1907-1920, 2009.

3 Bork, H. R. and Lang A.: Quantification of past soil erosion and land use / land cover changes in Germany, in: Long term hillslope and fluvial system modelling. Concepts and case studies from the Rhine river catchment, Lecture Notes in Earth Sc.,101, 231-239, 2003.

4 Cerdan, O., Govers, G., Le Bissonnais, Y., Van Oost, K., Poesen, J., Saby, N., Gobin, a., Vacca, a., Quinton, J., Auerswald, K., Klik, a., Kwaad, F. J. P. M., Raclot, D., Ionita, I., Rejman, J., Rousseva, S., Muxart, T., Roxo, M. J. and Dostal, T.: Rates and spatial variations of soil erosion in Europe: A study based on erosion plot data, Geomorphology, 122(1-2), 167–177, doi:10.1016/j.geomorph.2010.06.011, 2010.

5 Chang, K. T. and Tsai, B. W.: The effect of DEM resolution on slope and aspect mapping, Cartography and Geographic Information Systems, 18(1), 69-77, 1991.

6 Cooper K.: Evaluation of the Relationship between the RUSLE R-Factor and Mean Annual Precipitation, available at: http://www.engr.colostate.edu/~pierre/ce_old/Projects/linkfiles/Cooper%20R-factor-Final.pdf (last access: 15 January 2015), 2011.

7 Da Silva, A. M.: Rainfall erosivity map for Brazil, Catena, 57(3), 251–259, doi:10.1016/j.catena.2012.08.006, 2004.

8 De Jong, S. M., Brouwer, L. C. and Riezebos, H. Th.: Erosion hazard assessment in the Peyne catchment, France, Working paper DeMon-2 Project. Dept. Physical Geography, Utrecht University, 1998.

9 Diodato, N. and Bellocchi, G.: MedREM, a rainfall erosivity model for the Mediterranean region, J. Hydrol., 387(1-2), 119–127, doi:10.1016/j.jhydrol.2010.04.003, 2010.

10 Doetterl, S., Van Oost, K. and Six, J.: Towards constraining the magnitude of global agricultural sediment and soil organic carbon fluxes, Earth Surf. Process. Landforms, 37(6), 642–655, doi: 10.1002/esp.3198, 2012.

11 Donat, M. G., Alexander, L.V., Yang, H., Durre, I., Vose, R. and Caesar, J.: Global Land-Based Datasets for Monitoring Climatic Extremes, Bulletin American Meteorological Society, 94, 997–1006, available online at: http://dx.doi.org/10.1175/BAMS-D-12-00109.1 (last access: 15 January 2015), 2013.

12 Friedl, M. A., Strahler, A. H. and Hodges, J.: ISLSCP II MODIS (Collection 4) IGBP Land Cover, 2000-2001. In Hall, Forest G., G. Collatz, B. Meeson, S. Los, E. Brown de Colstoun, and D. Landis (eds.), ISLSCP Initiative II Collection, available online at: http://daac.ornl.gov/ (last access: 15 January 2015), from Oak Ridge National Laboratory Distributed Active Archive Center, Oak Ridge, Tennessee, U.S.A, 2010.

13 Gesch, D.B., Verdin, K.L. and Greenlee, S.K.: New land surface digital elevation model covers the earth, Eos, Transactions, AGU, 80(6), 69–70, doi: 10.1029/99EO00050, 1999.

14 Goll, D. S., Brovkin, V., Parida, B. R., Reick, C. H., Kattge, J., Reich, P. B., van Bodegom, P. M. and Niinemets, Ü.: Nutrient limitation reduces land carbon uptake in simulations with a model of combined carbon, nitrogen and phosphorus cycling, Biogeosciences, 9(9), 3547–3569, doi:10.5194/bg-9-3547-2012, 2012.

15 Goovaerts, P.: Using elevation to aid the geostatistical mapping of rainfall erosivity, Catena, 34, 227–242, doi: 10.1016/S0341-8162(98)00116-7, 1999.

16 Gruber, N. and Galloway, J. N.: An Earth-system perspective of the global nitrogen cycle, Nature, 451(7176), 293–6, doi:10.1038/nature06592, 2008.

17 Hall, F. G., Brown de Colstoun, E., Collatz, G. J., Landis, D., Dirmeyer, P., Betts, A., Huffman, G. J., Bounoua, L. and Meeson, B.: ISLSCP Initiative II global data sets: Surface boundary conditions and atmospheric forcings for land-atmosphere studies, J. Geophys. Res., 111(D22), D22S01, doi: 10.1029/2006JD007366, 2006.

18 Hooke, R. L.: On the history of humans as geomorphic agents, Geology, 28(9), 843–846, doi:10.1130/0091-7613, 2000.

19 Hudson N.: Soil Conservation, Cornell University Press, Ithaca, 1971.

20 Ito, A.: Simulated impacts of climate and land-cover change on soil erosion and implication for the carbon cycle, 1901 to 2100, Geophys. Res. Lett., 34(9), doi:10.1029/2007GL029342, 2007.

21 Klinkenberg, B. and Goodchild, M. F.: The fractal properties of topography: A comparison of methods, Earth Surf. Process. Landforms, 17(3), 217-234, doi: 10.1002/esp.3290170303, 1992.

22 Lal, R.: Soil erosion and the global carbon budget, Environ. Int., 29(4), 437–50, doi:10.1016/S0160-4120(02)00192-7, 2003.

23 Lohmann, U., Sausen, R., Bengtsson, L., Cubasch, U., Perlwitz, J. and Roeckner, E.: The Köppen climate classification as a diagnostic tool for general circulation models, Climate Res., 3, 177-193, 1993.

24 Meusburger, K., Steel, a., Panagos, P., Montanarella, L. and Alewell, C.: Spatial and temporal variability of rainfall erosivity factor for Switzerland, Hydrol. Earth Syst. Sci. Discuss., 8(5), 8291–8314, doi: 10.5194/hessd-8-8291-2011, 2011.

25 Meusburger, K., Steel, a., Panagos, P., Montanarella, L. and Alewell, C.: Spatial and temporal variability of rainfall erosivity factor for Switzerland, Hydrol. Earth Syst. Sci., 16(1), 167–177, doi: 10.5194/hess-16-167-2012, 2012.

26 Meyer-Christoffer, A., Becker, A., Finger, P., Rudolf, B., Schneider, U. and Ziese, M.: GPCC Climatology Version 2011 at 0.25°: Monthly Land-Surface Precipitation Climatology for Every Month and the Total Year from Rain-Gauges built on GTS-based and Historic Data, 2011.

27 Milliman, J. D. and Syvitski, J. P. M.: Geomorphic / Tectonic Control of Sediment Discharge to the Ocean : The Importance of Small Mountainous Rivers, J. Geology, 100(5), 525–544, 1992.

28 Mikhailova, E. A., Bryant, R. B., Schwager, S. J., and Smith, S. D.: Predicting rainfall erosivity in Honduras, Soil.Sci. Soc. Am. J., 61(1): 273-279, doi:10.2136/sssaj1997.03615995006100010039x, 1997.

29 Montgomery, D. R.: Soil erosion and agricultural sustainability, PNAS, 104(33), 13268–13272, doi: 10.1073/pnas.0611508104, 2007.

30 National Geophysical Data Center/NESDIS/NOAA/U.S. Department of Commerce: TerrainBase, Global 5 Arc-minute Ocean Depth and Land Elevation from the US National Geophysical Data Center (NGDC), Research Data Archive at the National Center for Atmospheric Research, Computational and Information Systems Laboratory, available online at: http://rda.ucar.edu/datasets/ds759.2/ (last access 30 November 2014), 1995.

31 Nearing, M.A.: A single, continues function for slope steepness influence on soil loss, Soil. Sci. Soc. Am. J., 61(3): 917-929, doi:10.2136/sssaj1997.03615995006100030029x, 1997.

32 Oliveira, P. T. S., Wendland, E. and Nearing, M. A.: Rainfall erosivity in Brazil: A review, Catena, 100, 139–147, doi:10.1016/j.catena.2012.08.006, 2013.

33 Peel, M. C., Finlayson, B. L. and Mcmahon, T. A.: Updated world map of the Köppen-Geiger climate classification, HESS, 1633–1644, 2007.

34 Pimentel, D., Harvey, C., Resosudarmo, P., Sinclair, K., Kurz, D., Mcnair, M., Cris, S., Shpritz, L., Fitton, L., Saffouri, R. and Blair, R.: Environmental and economic costs of soil erosion and conservation benefits, Science, 267(5201), 1117-1123, 1995.

35 Poesen, J. W., Torri, D., and Bunte, K.: Effects of rock fragments on soil erosion by water at different spatial scales: a review, Catena, *23*(1), 141-166, 1994.

36 Pradhan, N. R., Tachikawa, Y. and Takara, K.: A downscaling method of topographic index distribution for matching the scales of model application and parameter identification, Hydrol. Process., 20(6), 1385–1405, doi:10.1002/hyp.6098, 2006.

37 Quinton, J. N., Govers, G., Van Oost, K. and Bardgett, R. D.: The impact of agricultural soil erosion on biogeochemical cycling, Nat. Geosci., 3(5), 311–314, doi: 10.1038/ngeo838, 2010.

38 Regnier, P., Friedlingstein, P., Ciais, P., Mackenzie, F. T., Gruber, N., Janssens, I. A., Laruelle, G. G., Lauerwald, R., Luyssaert, S., Andersson, A. J., Arndt, S., Arnosti, C., Borges, A. V., Dale, A. W., Gallego-Sala, A., Goddéris, Y., Goossens, N., Hartmann, J., Heinze, C., Ilyina, T., Joos, F., LaRowe, D. E., Leifeld, J., Meysman, F. J. R., Munhoven, G., Raymond, P. a., Spahni, R., Suntharalingam, P. and Thullner, M.: Anthropogenic perturbation of the carbon fluxes from land to ocean, Nat. Geosci., 6(8), 597–607, doi:10.1038/ngeo1830, 2013.

39 Reich, P. B. and Hungate, B. A.: Carbon-Nitrogen in Terrestrial Interactions in Response Ecosystems to Rising Atmospheric Carbon Dioxide, Annu. Rev. Ecol. Evol. Syst., 37, 611–636, doi: 10.2307/annurev.ecolsys.37.091305.30000023, 2006.

40 Renard, K. G. and Freimund, J. R.: Using monthly precipitation data to estimate the R-Factor in the revised USLE, J. Hydrol.,157, 287-306, doi:10.1016/0022-1694(94)90110-4, 1994.

41 Renard, K. G., Foster, G. R., Weesies, G.A., Mccool, D. K. and Yoder, D. C.: Predicting Soil Erosion by Water: a Guide to Conservation Planning with the Revised Universal Soil Loss Equation (RUSLE), Agriculture Handbook 703, USDA, 1997.

42 Schneider, U., Becker, A., Finger, P., Meyer-Christoffer, A., Rudolf, B. and Ziese, M.: GPCC Full Data Reanalysis Version 6.0 at 0.5°: Monthly Land-Surface Precipitation from Rain-Gauges built on GTS-based and Historic Data, 2011.

43 Shangguan, W., Dai, Y., Duan, Q., Liu, B. and Yuan, H.: A Global Soil Data Set for Earth System Modeling, J. Adv. Model. Earth Syst., 6, 249-263, doi: 10.1002/2013MS000293, 2014.

44 Stallard, R. F.: Terrestrial sedimentation and the carbon cycle: Coupling weathering and erosion to carbon burial, Global Geochem. Cy., 12(2), 231–257, doi:10.1029/98GB00741, 1998.

45 Thornton, P. E., Lamarque, J.-F., Rosenbloom, N. a. and Mahowald, N. M.: Influence of carbon-nitrogen cycle coupling on land model response to CO 2 fertilization and climate variability, Global Biogeochem. Cycles, 21(4), n/a–n/a, doi: 10.1029/2006GB002868, 2007.

46 Torri, D., Poesen, J. and Borselli, L.: Predictability and uncertainty of the soil erodibility factor using a global dataset, Catena, 31, 1-22, doi:10.1016/S0341-8162(97)00036-2, 1997.

47 Tucker, C., Pinzon, J., Brown, M., Slayback, D., Pak, E., Mahoney, R., Vermote, E. and El Saleous, N.: An extended AVHRR 8-km NDVI dataset compatible with MODIS and SPOT vegetation NDVI data, Int. J. Remote Sens., 26(20), 4485–4498, 2005.

48 United Nations Convention to Combat Desertification (UNCCD): Zero Net Land Degradation, 2012.

49 United States Environmental Protection Agency: Stormwater Phase 2 Final Rusle, Construction Rainfall Erosivity Waiver, EPA 833-F-00-014, 2001.

50 US Department of Agriculture: Summary Report: 1997 National Resources Inventory (revised December 2000), Natural Resources Conservation Service, Washington, DC, and Statistical Laboratory, Iowa State University, Ames, Iowa, 2000.

51 US Department of Commerce, National Oceanic and Atmospheric Adminis.: 2-minute Gridded Global Relief Data (ETOPO2), 2001.

52 US Geological Survey: GTOPO30 Arc-Second Elevation Data Set, EROS Data Center (EDC) Distributed Active Archive Center (DAAC), Sioux Falls, available online at: http://edcdaac.usgs.gov/gtopo30/gtopo30.html (last access 15 January 2015), 1996.

53 Van der Knijff, J. M., Jones, R. J. A. and Montanarella, L.: Soil Erosion Risk Assessment in Italy, Joint Research Center, EUR19022EN, European Commission, 1999.

54 Van Oost, K., Quine, T. a, Govers, G., De Gryze, S., Six, J., Harden, J. W., Ritchie, J. C., McCarty, G. W., Heckrath, G., Kosmas, C., Giraldez, J. V, da Silva, J. R. M. and Merckx, R.: The impact of agricultural soil erosion on the global carbon cycle, Science, 318(5850), 626–9, doi:10.1126/science.1145724, 2007.

55 Walling, D.E.: The Impact of Global Change on Erosion and Sediment Transport by Rivers: Current Progress and Future Challenges. The United Nations World Water Assessment Programme Scientific Paper, UNESCO, Paris, 2009

56 Wilkinson, B. H. and McElroy, B. J.: The impact of humans on continental erosion and sedimentation, Geol. Soc. Am. Bull., 119(1-2), 140–156, doi:10.1130/B25899.1, 2007.

57 Wischmeier, W. H. and Smith, D. D.: Predicting Rainfall Erosion Losses. A guide to conservation planning, Agricultural Handbook 537, USDA, Washington, 58 pp, 1978.

58 Yang, D., Kanae, S., Oki, T., Koike, T. and Musiake, K.: Global potential soil erosion with reference to land use and climate changes, Hydrol. Process., 17, 2913–2928, doi:10.1002/hyp.1441, 2003.

59 Zhang, W. and Montgomery, D. R.: Digital elevation model grid size, landscape representation, and hydrologic simulations, Water Resour. Res., 30(4), 1019-1028, doi:10.1029/93WR03553, 1994.

60 Zhang, X., Drake, N. and Wainwright, J.: Scaling land surface parameters for global-scale soil erosion estimation, Water Resour. Res., 38, 19–1–19–9, doi:10.1029/2001WR000356, 2002.

61 Zhang, X., Drake, N. A., Wainwright, J. and Mulligan, M.: Comparison of slope estimates from low resolution DEMs: Scaling issues and a fractal method for their solution, Earth Surf. Processes Landforms, 14, 763–779, 1999.

Table 1. List of datasets used in this study

Category	Dataset	Source	Spatial resolution	Temporal-period	Variables
DEM	GTOPO Elevation Model	USGS, 1996, Gesch *et al.*, 1999	30 arc-seconds		elevation
	ETOPO1 Elevation Model	Amante and Eakins, 2009	1 arc-minute		elevation
	ETOPO2 Elevation Model	US Department of Commerce and NOAA, 2001	2 arc-minute		elevation
	ETOPO5 Elevation Model	National Geophysical Data Center/NESDIS/NOAA, 1995	5 arc-minute		elevation
Climate	GPCC 0.5 degree dataset	Schneider *et al.*, 2011	0.5 degrees	Years 1989-2010	total yearly precipitation
	GPCC 0.25 degree	Meyer-Christoffer *et al.*,	0.25 degrees	years 1951-	total yearly

	dataset	2011		2000	precipitation
	GHCNDEX dataset	CLIMDEX (Donat *et al.*, 2013)	2.5 degrees	years 1951-present	simple precipitation intensity index (SDII)
	Köppen-Geiger dataset	Peel *et al.*, 2007	5 arc-minute		Köppen-Geiger climate classifications
Soil	Global Soil Dataset for use in Earth System Models (GSCE)	Shangguan *et al.*, 2014	30 arc-seconds		sand, silt and clay fractions, organic matter %, gravel %
	Harmonized World Soil Database (HWSD) version 1.2	Nachtergaele *et al.*, 2012	30 arc-seconds		volcanic soils
Land-cover	GIMMS dataset	ISLSCP II (Tucker *et al.*, 2005, Hall *et al.*, 2006	0.25 degrees	year 2002	Normalized difference vegetation index (NDVI)
Land-use	MODIS dataset	ISLSCP II (Friedl *et al.*, 2010, Hall *et al.*, 2006)	0.25 degrees	year 2002	Land use fractions

Table 2. Fractal parameters and the resulting mean global slopes before and after applying the fractal method on the different DEMs; Increase of slope means the increase of the average global slope of a DEM after applying the fractal method; difference after scaling $=\frac{\theta_{scaled(DEM)} - \theta_{scaled(GTOPO30)}}{\theta_{scaled(GTOPO30)}} * 100$; difference before scaling $=\frac{\theta_{(DEM)} - \theta_{(GTOPO30)}}{\theta_{(GTOPO30)}} * 100$

DEM	resolution	standard deviation of elevation	mean D	mean $\alpha_{steepest}$	θ	θ_{scaled}	Increase of θ	difference after scaling	difference before scaling
	arc-minute	m			m m-1	m m-1	%	%	%
GTOPO30	0.5	570	1.32	0.99	0.023	0.059	61	0	0
ETOPO1	1	530	1.35	1.08	0.016	0.057	71.9	-3.4	-30.4
ETOPO2	2	549	1.37	1.17	0.011	0.055	80	-6.8	-52.2
ETOPO5	5	562	1.42	1.25	0.006	0.054	88.9	-8.5	-73.9

Table 3. Description of Köppen climate symbols and defining criteria (from Peel *et al.*, 2007).

1st	2nd	3rd	Description	Criteria*
A			Tropical	$T_{cold}>=18$
	f		- Rainforest	$P_{dry}>=60$
	m		- Monsoon	Not (Af) & $P_{dry}>=100–MAP/25$
	w		- Savannah	Not (Af) & $P_{dry}<100–MAP/25$
B			Arid	$MAP<10×P_{threshold}$
	W		- Desert	$MAP<5×P_{threshold}$
	S		- Steppe	$MAP>=5×P_{threshold}$
		h	▪ Hot	$MAT>=18$
		k	▪ Cold	$MAT<18$
C			Temperate	$T_{hot>}10\&0<T_{cold}<18$
	s		- Dry Summer	$P_{sdry}<40\&P_{sdry}<P_{wwet}/3$
	w		- Dry Winter	$P_{wdry}<P_{swet}/10$
	f		- Without dry season	Not (Cs) or (Cw)
		a	▪ Hot Summer	$T_{hot}>=22$
		b	▪ Warm Summer	Not (a) & $T_{mon10}>=4$
		c	▪ Cold Summer	Not (a or b) & $1<=T_{mon10}<4$
D			Cold	$T_{hot}>10\&T_{cold}<=0$
	s		- Dry Summer	$P_{sdry}<40\&P_{sdry}<P_{wwet}/3$
	w		- Dry Winter	$P_{wdry}<P_{swet}/10$
	f		- Without dry season	Not (Ds) or (Dw)
		a	▪ Hot Summer	$T_{hot}>=22$
		a	▪ Warm Summer	Not (a) & $T_{mon10}>=4$
		c	▪ Cold Summer	Not (a, b or d)
		d	▪ Very Cold Winter	Not (a or b) & $T_{cold}<=-38$
E			Polar	$T_{hot}<10$
	T		- Tundra	$T_{hot}>0$
	F		- Frost	$T_{hot}<-0$

***** MAP = mean annual precipitation, MAT = mean annual temperature, T_{hot} = temperature of the hottest month, T_{cold} = temperature of the coldest month, T_{mon10} = number of months where the temperature is above 10, P_{dry} = precipitation of the driest month, P_{sdry} = precipitation of the driest month in summer, P_{wdry} = precipitation of the driest month in winter, P_{swet} = precipitation of the wettest month in summer, P_{wwet} = precipitation of the wettest month in winter, $P_{threshold}$ = varies according to the following rules (if 70% of MAP occurs in winter then $P_{threshold}$ = 2 x MAT, if 70% of MAP occurs in summer then $P_{threshold}$ = 2 x MAT + 28, otherwise $P_{threshold}$ = 2 x MAT + 14). Summer (winter) is defined as the warmer (cooler) six month period of ONDJFM and AMJJAS.

Table 4. Linear multiple regression equations for different climate zones, relating high resolution R factor from the USA with one or more significant parameters: annual total mean precipitation, *P* (mm), mean elevation, *z* (m), and the simple precipitation intensity index, *SDII* (mm/day).

Climate zone	Explaining parameters	Regression function - optimal	R^2	Residual standard error
BWk	P, SDII	$R = 0.809 * P^{0.957} + 0.000189 * SDII^{6.285}$		
BSh	P, SDII	$\log R = -7.72 + 1.595 * \log P + 2.068 * \log SDII$	0.97	0.22
BSk	P, SDII, Z	$\log R = 0.0793 + 0.887 * \log P + 1.892 * \log SDII - 0.429 * \log Z$	0.89	0.35
Csb	P	$R = 98.35 + 0.000355 * P^{1.987}$		0.16
Cfa	P, SDII, Z	$\log R = 0.524 + 0.462 * \log P + 1.97 * \log SDII - 0.106 * \log Z$	0.89	0.11
Cfb	P, SDII	$\log R = 4.853 + 0.676 * \log P + 3.34 * \log SDII$	0.97	0.21
Dsa	Z, SDII	$\log R = 8.602 - 0.963 * \log SDII - 0.247 * \log Z$	0.51	0.05
Dsb	P	$\log R = 2.166 + 0.494 * \log P$	0.45	0.25
Dsc	SDII	$\log R = 6.236 - 0.869 * \log SDII$	0.51	0.02
Dwa	P	$\log R = -0.572 + 1.238 * \log P$	0.99	0.02
Dwb	P, SDII	$\log R = -1.7 + 0.788 * \log P + 1.824 * \log SDII$	0.98	0.02
Dfa	P, SDII	$\log R = -1.99 + 0.737 * \log P + 2.033 * \log SDII$	0.9	0.16
Dfb	P, SDII, Z	$\log R = -0.5 + 0.266 * \log P + 3.1 * \log SDII - 0.131 * \log Z$	0.89	0.32
Dfc	SDII	$\log R = -1.259 + 3.862 * \log SDII$	0.91	0.23
ET	P	$\log R = -3.945 + 1.54 * \log P$	0.14	0.42

EF+EFH	P	$\log R = 16.39 - 1.286 * \log P$	0.6	0.13
ETH	P, SDII	$\log R = 21.44 + 1.293 * \log P - 10.579 * \log SDII$	0.52	0.53

Table 5. Linear multiple regression equations for different climate zones for regions that have no data on the simple precipitation intensity index, *SDII* (mm/day). The regression equations relate high resolution erosivity from the USA with the annual total mean precipitation, *P* (mm), and/or the mean elevation, *z* (m).

Climate zone	Optimal regression function (when SDII is not available)	R^2	Residual standard error
BWk	Method Renard & Freimund (1994)		
BSh	$\log R = -8.164 + 2.455 * \log P$	0.86	0.5
BSk	$\log R = 5.52 + 1.33 * \log P - 0.977 * \log Z$	0.76	0.52
Cfa	$\log R = 3.378 + 0.852 * \log P - 0.191 * \log Z$	0.57	0.23
Cfb	$\log R = 5.267 + 0.839 * \log P - 0.635 * \log Z$	0.81	0.5
Dsa	$\log R = 7.49 - 0.0512 * \log P - 0.272 * \log Z$	0.48	0.06
Dsc	$\log R = 4.416 - 0.0594 * \log P$	0.015	0.03
Dwb	$\log R = 1.882 + 0.819 * \log P$	0.81	0.08
Dfa	$\log R = -2.396 + 1.5 * \log P$	0.65	0.29
Dfb	$\log R = 1.96 + 1.084 * \log P - 0.34 * \log Z$	0.74	0.48
Dfc	$\log R = -3.263 + 1.576 * \log P$	0.56	0.49
ETH	$\log R = -10.66 + 2.43 * \log P$	0.4	0.59

Table 6. Mean high resolution *R* values (MJ mm ha^{-1} h^{-1} year^{-1}) from the USA and Switzerland and mean modelled *R* values with uncertainty range for each addressed climate zone

climate	observed *R* mean	Renard & Freimund method *R mean*	adjusted method *R* mean	Adjusted method uncertainty range
BWk	284	533	291	158-495
BSh	2168	1356	2207	1723-2828
BSk	876	884	885	749-1046
Csb	192	1136	192	133-292
Cfa	5550	5607	5437	4830-6123
Cfb	1984	5359	1971	1431-2715
Dsa	172	445	171	86-340
Dsb	175	896	168	151-187
Dsc	115	374	115	91-145
Dwa	1549	1444	1551	1280-1879
Dwb	1220	1418	1214	1057-1395
Dfa	2572	2983	2582	2346-2843
Dfb	1101	1798	1124	922-1371
Dfc	483	701	483	423-552
ET	1352	6257	1249	23-68088
EF+EFH	1468	5469	1450	16-132001
ETH	945	5580	832	0-6314918

Table 7. Statistics of the comparison of high resolution R values (MJ mm ha^{-1} h^{-1} $year^{-1}$) from three regions to estimated R values from the Renard and Freimund method and the new regression equations

	Observed			Estimated – Renard & Freimund					Estimated – multiple linear regression				
	Range	Mean	Standard deviation	Range	Mean	Standard deviation	Correlation coefficient	Rank correlation coefficient	Range	Mean	Standard deviation	Correlation coefficient	Rank correlation coefficient
Switzerland	121-6500	1204	833	2335-10131	5798	1654	0.51	0.42	225-2572	1256	472	0.49	0.3
the USA (aggregated huc4)	105-4963	1271	1174	57-15183	1870	2088	0.51	0.68	60-15808	1691	2188	0.58	0.83
Ebro basin	40 - 4500	891	622	747 - 5910	1529	846	-	-	167 - 4993	836	701	-	-

Table 8. Comparison of the global erosion rates (t ha^{-1} $year^{-1}$) and percentiles between different versions of the RUSLE model

	mean	25th percentile	50th percentile	75th percentile	90th percentile
RUSLE unadjusted	4.5	0.2	0.7	2.4	7.5
RUSLE adjusted with S	9.8	0.3	1.0	3.8	13.5
RUSLE adjusted with R	3.2	0.1	0.5	1.7	5.7
RUSLE adjusted with S & R	6.5	0.1	0.7	2.7	9.6

Table 9. Statistics of the observed and modelled erosion rates from the unadjusted and adjusted versions of the RUSLE for the USA and Europe (t ha^{-1} $year^{-1}$)

Region	Source	Observations			Adjusted RUSLE			Unadjusted RUSLE		
		Range	Mean	Standard deviation	Range	Mean	Standard deviation	Range	Mean	Standard deviation
Europe (Aggregation country level) no small countries	Cerdan *et al.*, 2010	0.1-2.6	0.9	0.7	0.1-7	2.3	2.1	0-14	2.8	3.6
the USA (Aggregation HUC4 level)	NRI database	0-11	1.6	2.1	0.2-13	1.6	1.9	0-14	1.4	1.8

Figure 1. Global average unscaled slope estimated from different coarse resolution digital elevation models (DEMs) as function of their resolution (blue); and global average scaled slope from the same DEMs as function of their resolution (red).

Figure 2. (A) A global map of the scaled slope derived from the 30 arc-second DEM using a target resolution of 150m; (B) A global map showing the difference between the unscaled and scaled slopes (in degrees), where blue colours show an underestimation by the unscaled slope when compared to the scaled slope and reddish colours show and overestimation.

Figure 3. Spatial difference plots showing the difference between the high resolution *R* values and *R* values calculated with the method of Renard and Freimund for (A) the USA, (B) Switzerland and (C) the Ebro basin in Spain; In (A) and (B) the blue colours show an underestimation of the calculated *R* factor when compared to the high resolution *R* values, while the red colours show an overestimation; the Ebro basin serves here as an independent validation set and it has two graphs, (C1) a spatial plot of erosivity according to Renard and Freimund, and (C2) the high resolution *R* values from Angulo-Martinez *et al.* (2009); All values in the graphs are in MJ mm ha^{-1} h^{-1} $year^{-1}$.

Figure 4. The Köppen-Geiger climate classification global map at a resolution of 5 arc-minute (Peel *et al*., 2007).

Figure 5. Comparison of high resolution *R* factor data and predicted *R* values from (1) the Renard and Freimund method and (2) the new regression equations, for various climate zones;

the red line is the 1 tot 1 line, and does not appear in some graphs because predicted *R* values are overestimated.

Figure 6. Spatial difference plots showing the difference between the high resolution *R* values and *R* values calculated with the new regression equations for (A) the USA, (B) Switzerland and (C) the Ebro basin in Spain; In (A) and (B) the blue colours show an underestimation of the calculated *R* values when compared to the high resolution *R* values, while the red colours show an overestimation; the Ebro basin serves here as an independent validation set and it has two graphs, (C1) a spatial plot of the *R* factor according to the new regression equations, and (C2) the high resolution *R* values from Angulo-Martinez et al. (2009); All values in the graphs are in MJ mm ha^{-1} h^{-1} year^{-1}.

Figure 7. (A) Global distribution of the new modelled *R* values according to the new regression equations; and (B) a difference map between *R* values calculated according to the method of Renard and Freimund and the new modelled *R* values (MJ mm ha^{-1} h^{-1} year^{-1}), where blue colours indicate lower *R* values by Renard and Freimund compared to the new modelled *R* values, while redish colours indicate higher *R* values; map resolution is 5 arc-minute.

Figure 8. (A) Global yearly averaged erosion rates according to the fully adjusted RUSLE model; (B) a difference map between the fully adjusted and unadjusted RUSLE model; (C) a difference map between the adjusted S RUSLE and the unadjusted RUSLE model; (D) a difference map between the adjusted R RUSLE and the unadjusted RUSLE model; in figures B,C and D the reddish colors show an overestimation of by the adjusted RUSLE model and

yellow to bluish colors show an underestimation; resolution of all maps is 5 arc-minute and all units are in t ha^{-1} year^{-1}.

Figure 9. (A) Difference plots between soil erosion estimates from the NRI database for the USA and estimates of (A1) the unadjusted RUSLE model, and of (A2) the adjusted RUSLE model; all aggregated at HUC4 watershed level; (B) Difference plots between soil erosion estimates from the database of Cerdan *et al.* (2010) for Europe and estimates of (B1) the unadjusted RUSLE model and of (B2) the adjusted RUSLE model; all aggregated at country level; reddish colors represent an overestimation (t ha^{-1} year^{-1}) while the bluish represent and underestimation (t ha^{-1} year^{-1}) compared to the erosion values from the databases.

Figure 1

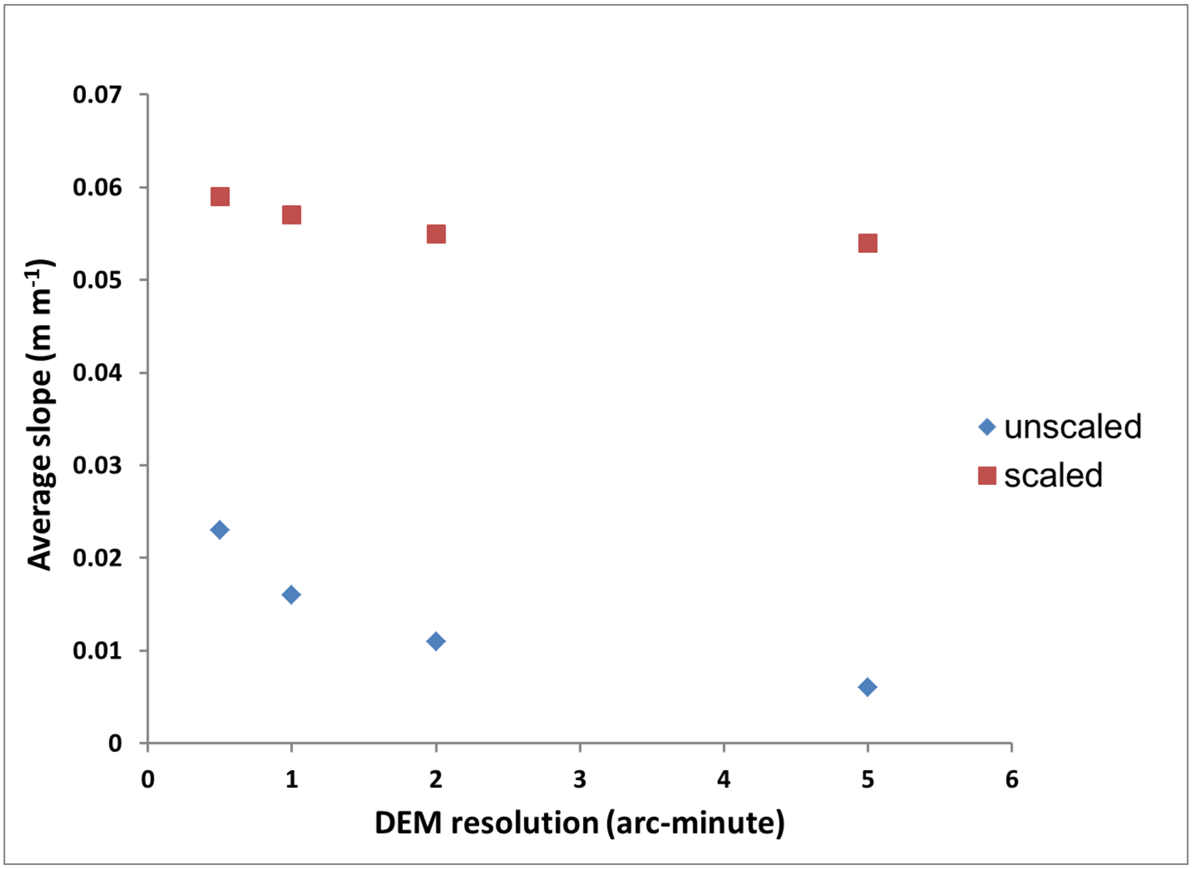
0.07
0.06
0.05
0.04
0.03
0.02
0.01
0
0
1
2
3
4
5
6
Average slope (m m-1)
DEM resolution (arc-minute)
unscaled
scaled

Figure 2

(A)

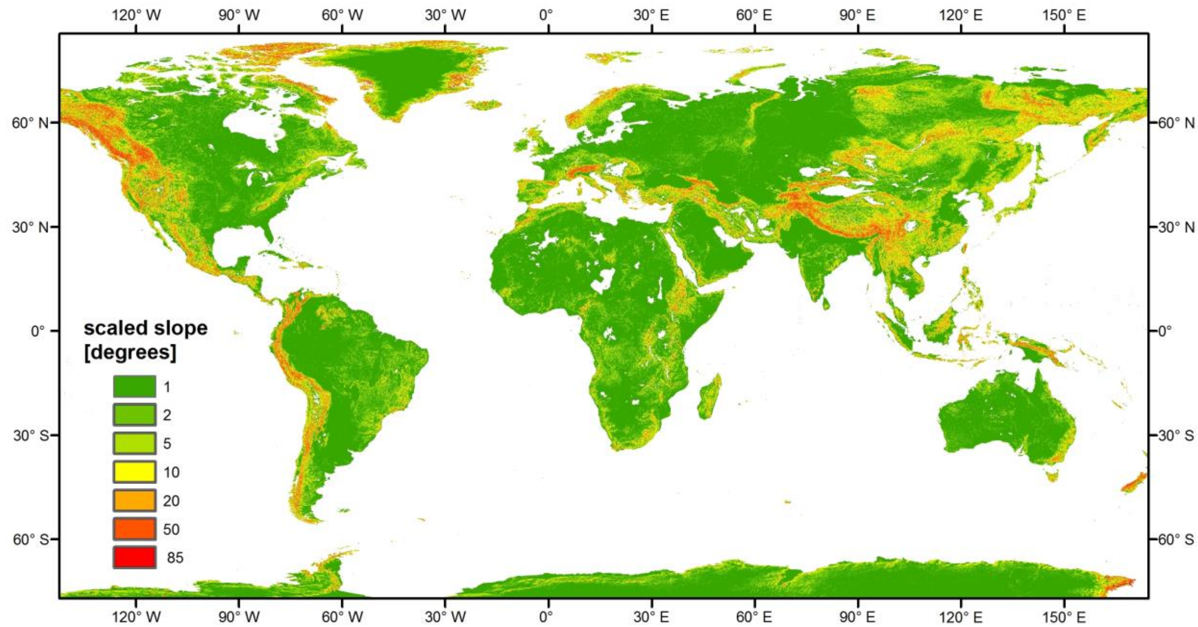
scaled slope
[degrees]
1
2
5
10
20
50
85
120° W
90° W
60° W
30° W
0°
30° E
60° E
90° E
120° E
150° E
60° N
30° N
0°
30° S
60° S

(B)

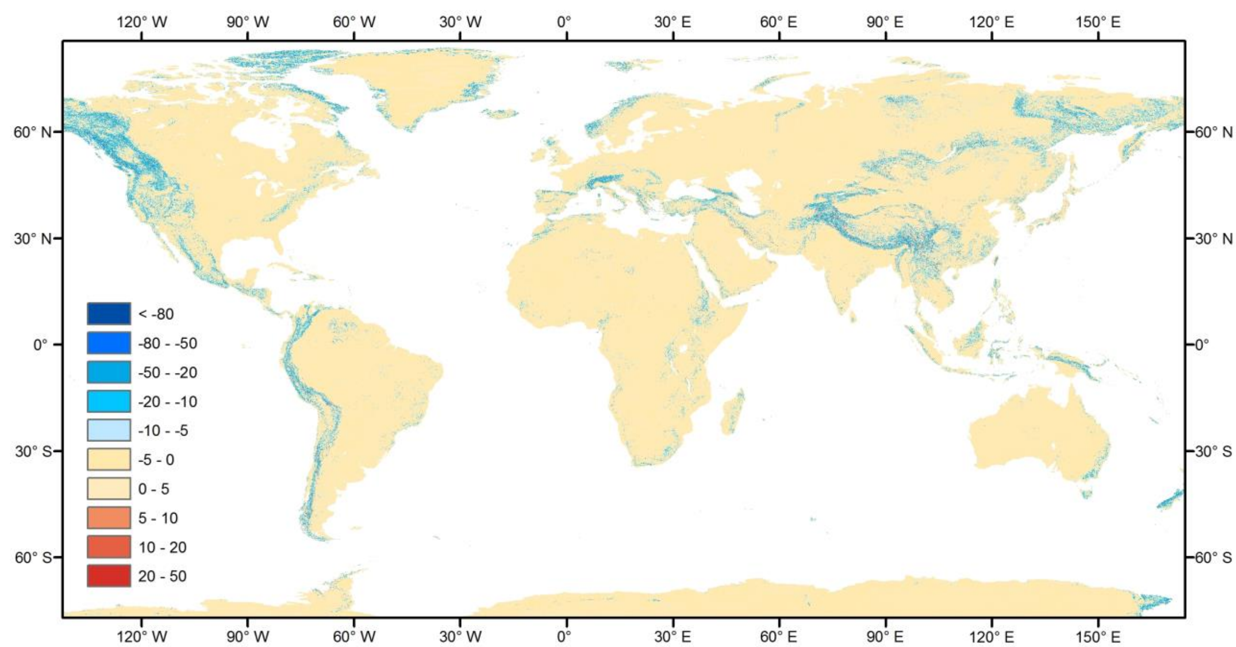
< -80
-80 - -50
-50 - -20
-20 - -10
-10 - -5
-5 - 0
0 - 5
5 - 10
10 - 20
20 - 50
120° W
90° W
60° W
30° W
0°
30° E
60° E
90° E
120° E
150° E
60° N
30° N
0°
30° S
60° S

Figure 3

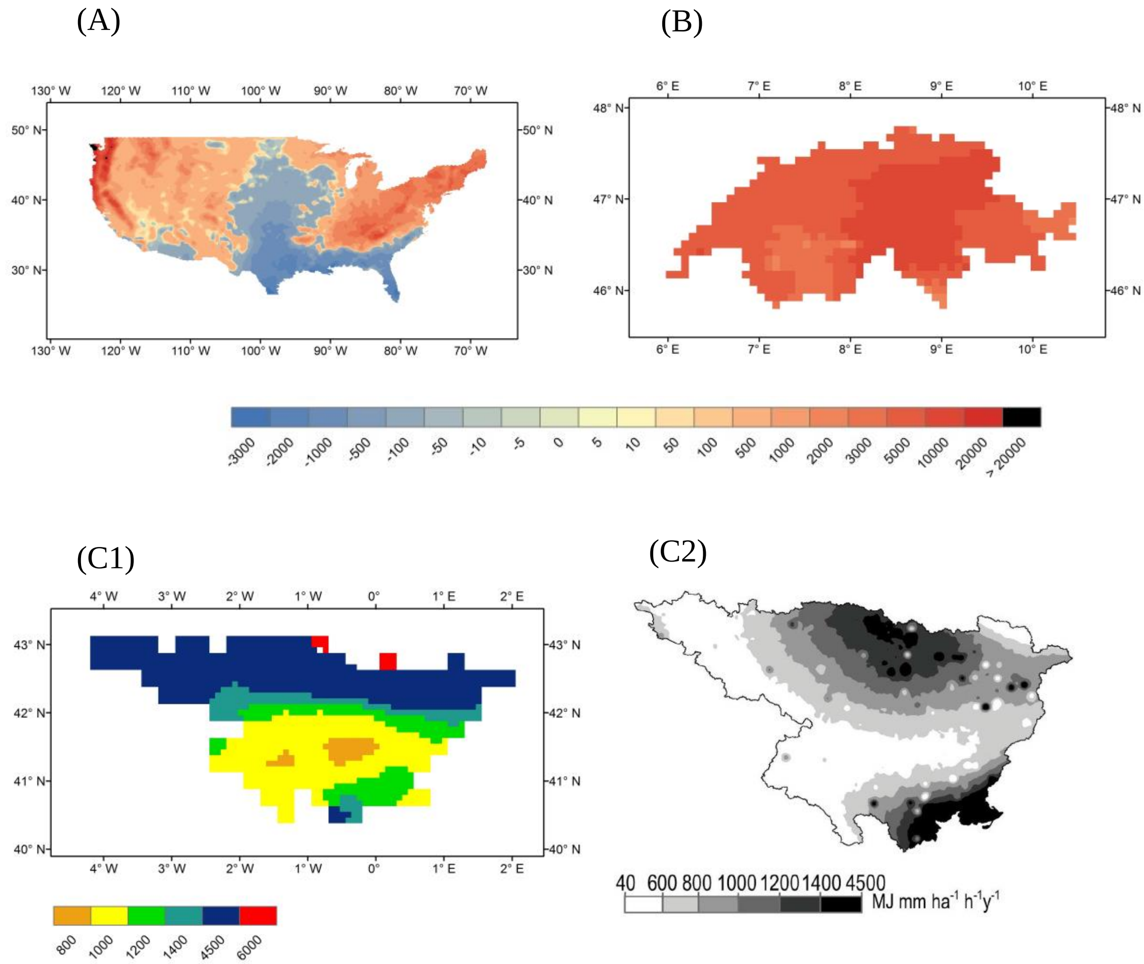
(A)
(B)
130° W 120° W 110° W 100° W 90° W 80° W 70° W
50° N 40° N 30° N
6° E 7° E 8° E 9° E 10° E
48° N 47° N 46° N
-3000 -2000 -1000 -500 -100 -50 -10 -5 0 5 10 50 100 500 1000 2000 3000 5000 10000 20000 > 20000
(C1)
(C2)
4° W 3° W 2° W 1° W 0° 1° E 2° E
43° N 42° N 41° N 40° N
800 1000 1200 1400 4500 6000
40 600 800 1000 1200 1400 4500
MJ mm ha^{-1} h^{-1}y^{-1}

Figure 4

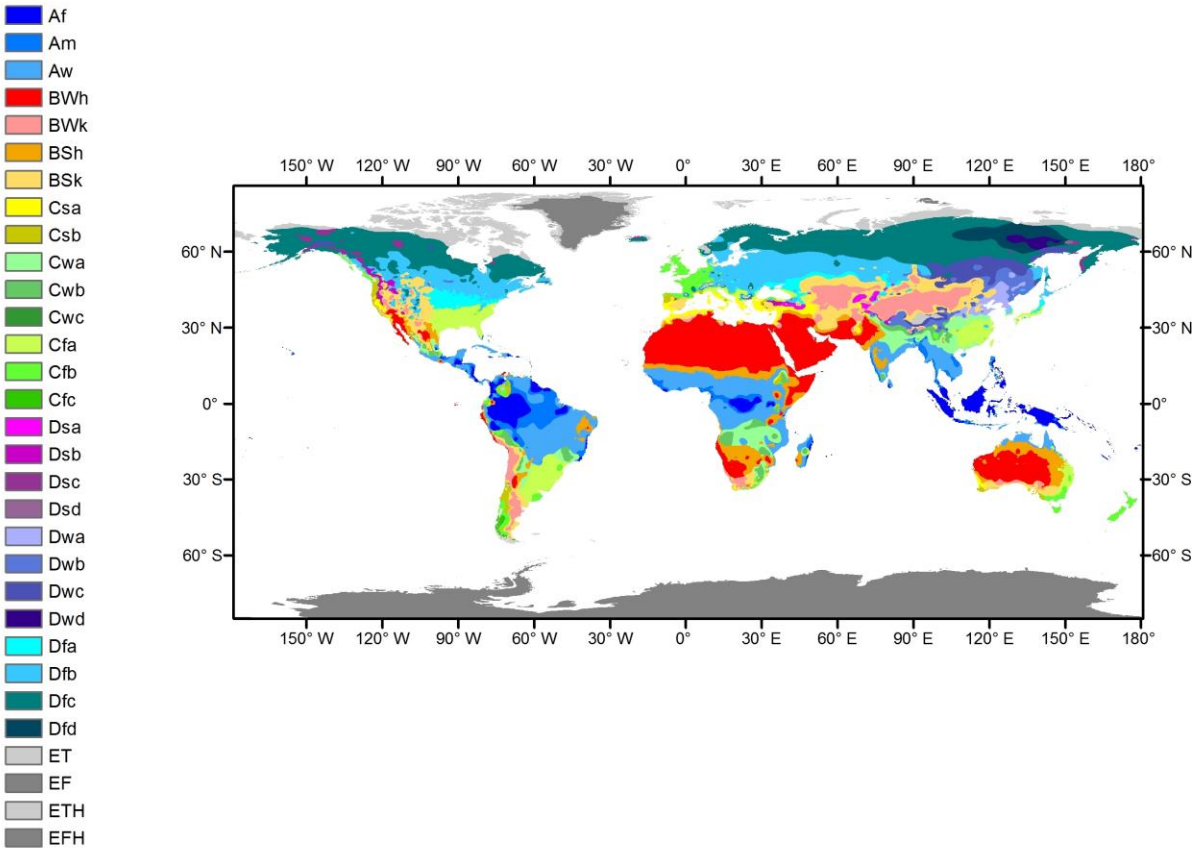

Af
Am
Aw
BWh
BWk
BSh
BSk
Csa
Csb
Cwa
Cwb
Cwc
Cfa
Cfb
Cfc
Dsa
Dsb
Dsc
Dsd
Dwa
Dwb
Dwc
Dwd
Dfa
Dfb
Dfc
Dfd
ET
EF
ETH
EFH
150° W
120° W
90° W
60° W
30° W
0°
30° E
60° E
90° E
120° E
150° E
180°
60° N
30° N
0°
30° S
60° S

Figure 5

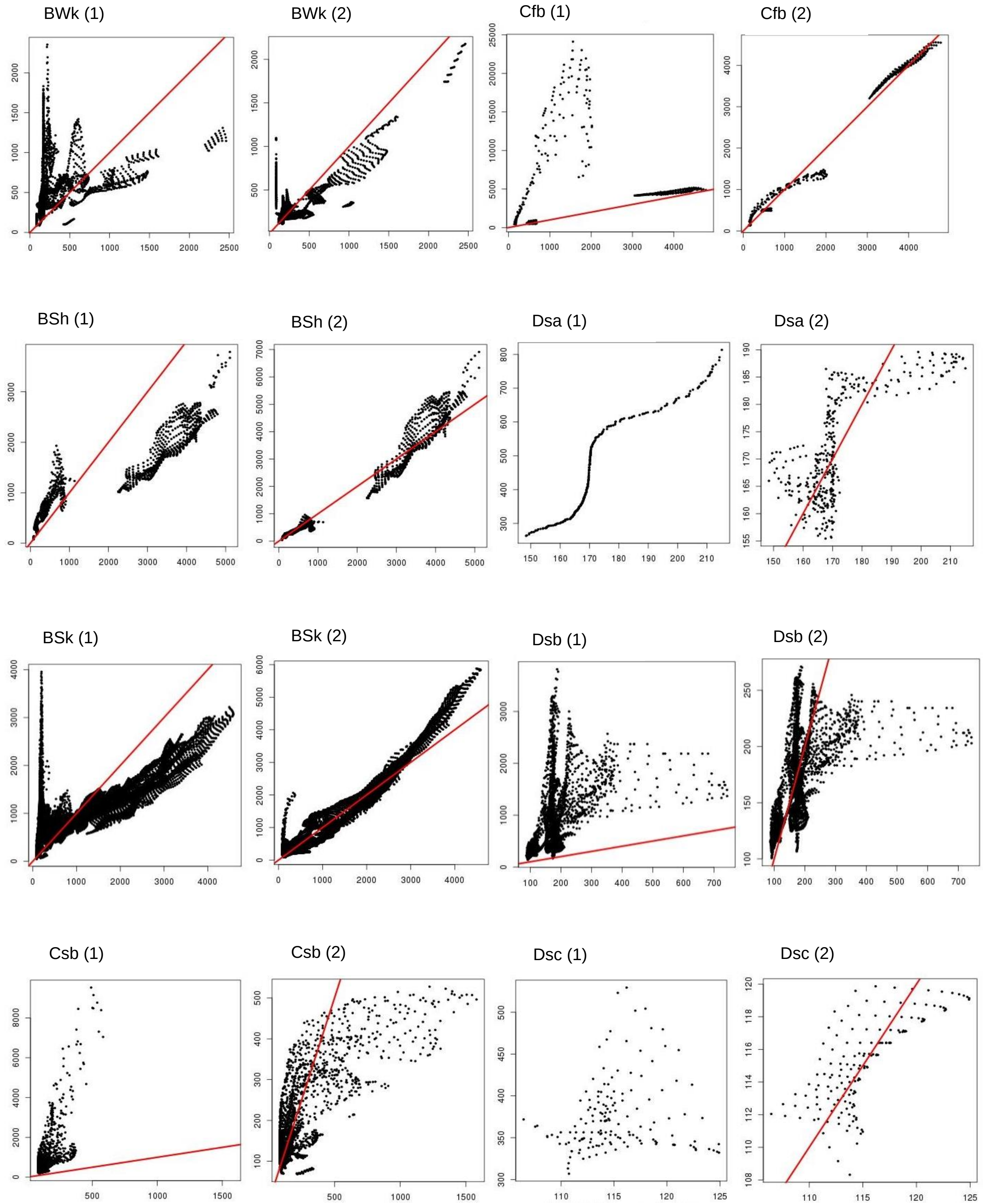
BWk (1)
BWk (2)
Cfb (1)
Cfb (2)
BSh (1)
BSh (2)
Dsa (1)
Dsa (2)
BSk (1)
BSk (2)
Dsb (1)
Dsb (2)
Csb (1)
Csb (2)
Dsc (1)
Dsc (2)

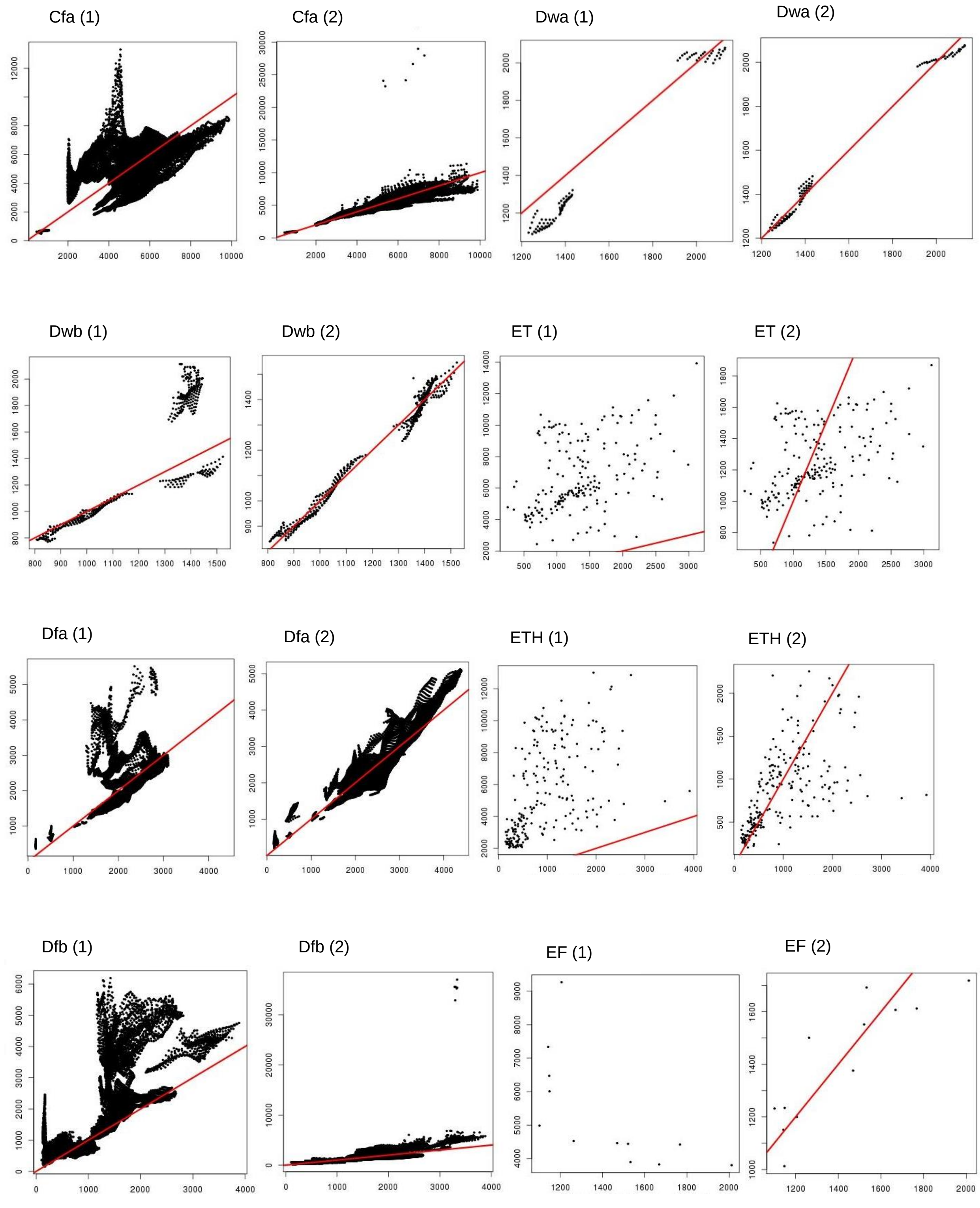
Cfa (1)
Cfa (2)
Dwa (1)
Dwa (2)
Dwb (1)
Dwb (2)
ET (1)
ET (2)
Dfa (1)
Dfa (2)
ETH (1)
ETH (2)
Dfb (1)
Dfb (2)
EF (1)
EF (2)

Dfc (1)

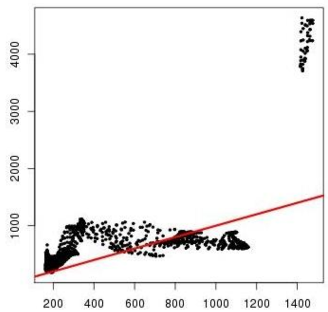

4000
3000
2000
1000
200
400
600
800
1000
1200
1400

Dfc (2)

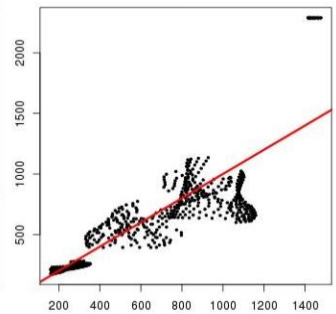

2000
1500
1000
500
200
400
600
800
1000
1200
1400

Figure 6

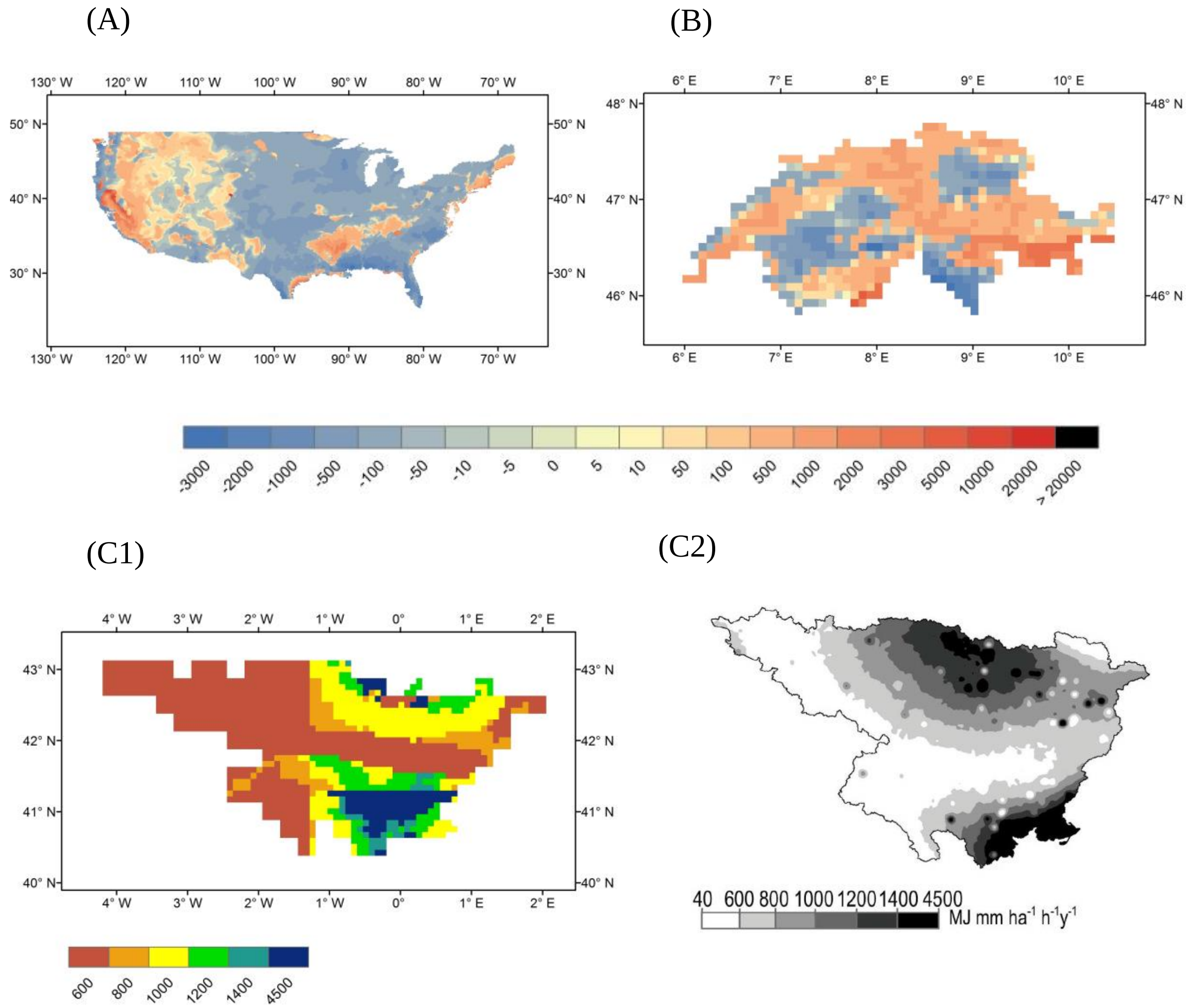
(A)
(B)
130° W
120° W
110° W
100° W
90° W
80° W
70° W
50° N
40° N
30° N
6° E
7° E
8° E
9° E
10° E
48° N
47° N
46° N
-3000
-2000
-1000
-500
-100
-50
-10
-5
0
5
10
50
100
500
1000
2000
3000
5000
10000
20000
> 20000
(C1)
(C2)
4° W
3° W
2° W
1° W
0°
1° E
2° E
43° N
42° N
41° N
40° N
600
800
1000
1200
1400
4500
40 600 800 1000 1200 1400 4500
MJ mm ha-1 h-1y-1

Figure 7

(A)

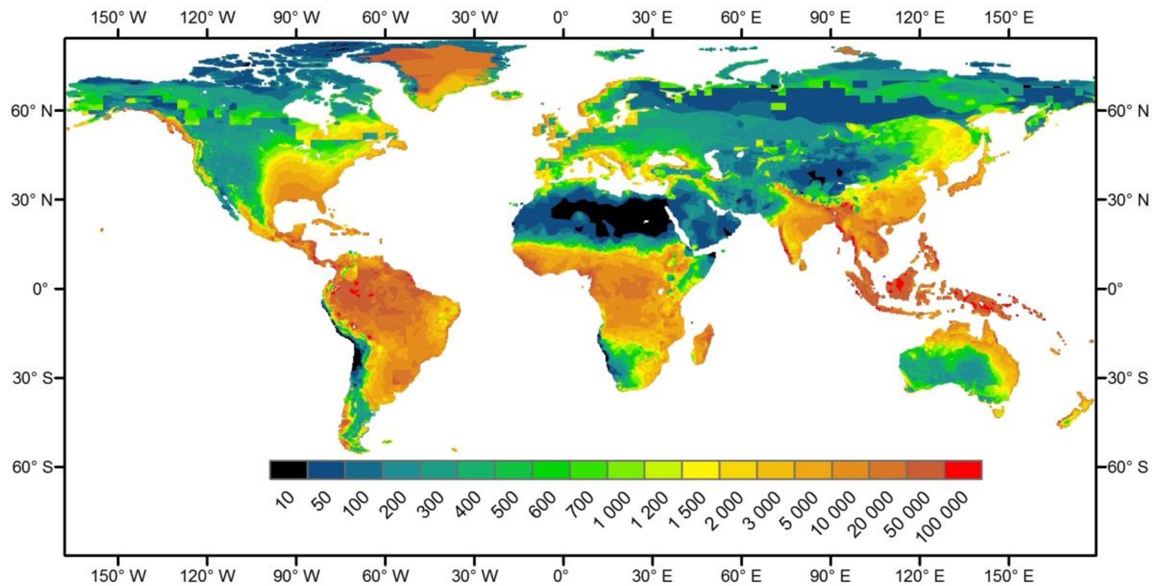
150° W
120° W
90° W
60° W
30° W
0°
30° E
60° E
90° E
120° E
150° E
60° N
30° N
0°
30° S
60° S
10
50
100
200
300
400
500
600
700
1 000
1 200
1 500
2 000
3 000
5 000
10 000
20 000
50 000
100 000

(B)

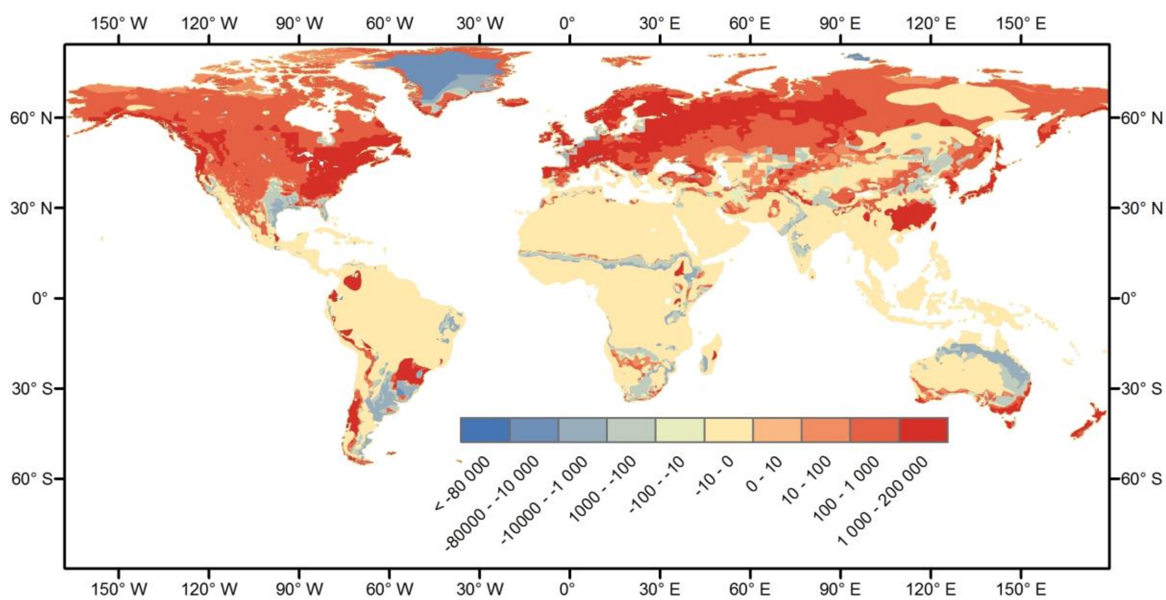
150° W
120° W
90° W
60° W
30° W
0°
30° E
60° E
90° E
120° E
150° E
60° N
30° N
0°
30° S
60° S
< -80 000
-80000 - -10 000
-10000 - -1 000
1000 - -100
-100 - -10
-10 - 0
0 - 10
10 - 100
100 - 1 000
1 000 - 200 000

(A) **Figure 8**

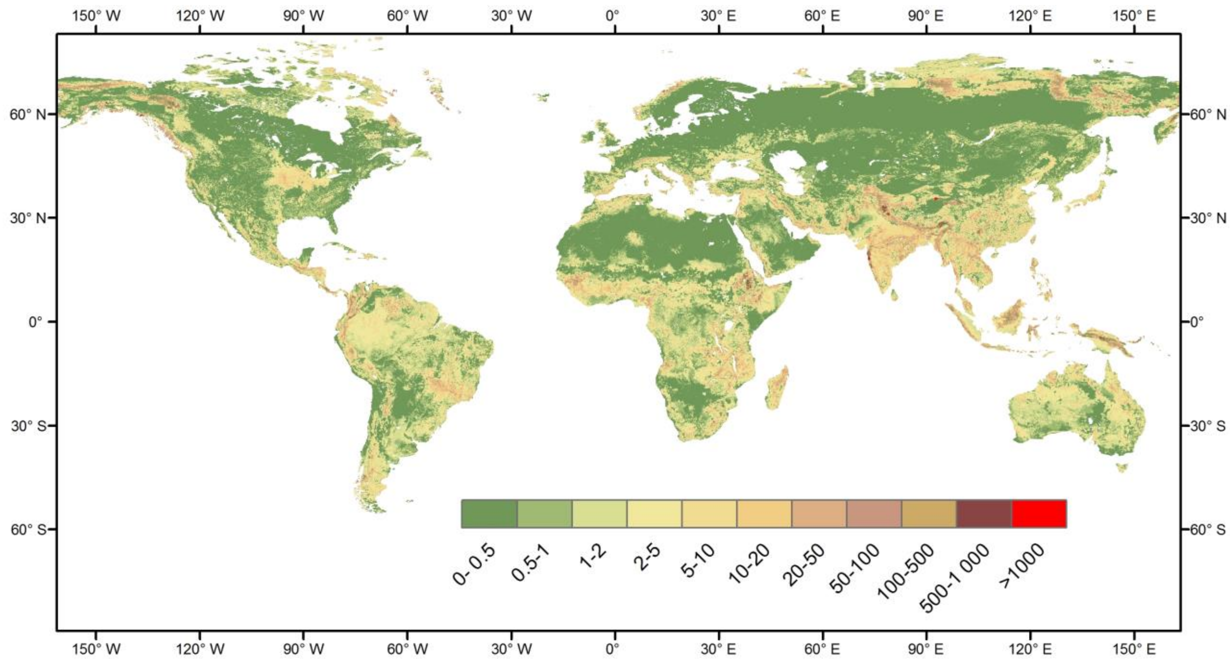

150° W
120° W
90° W
60° W
30° W
0°
30° E
60° E
90° E
120° E
150° E
60° N
30° N
0°
30° S
60° S
0- 0.5
0.5-1
1-2
2-5
5-10
10-20
20-50
50-100
100-500
500-1 000
>1000

(B)

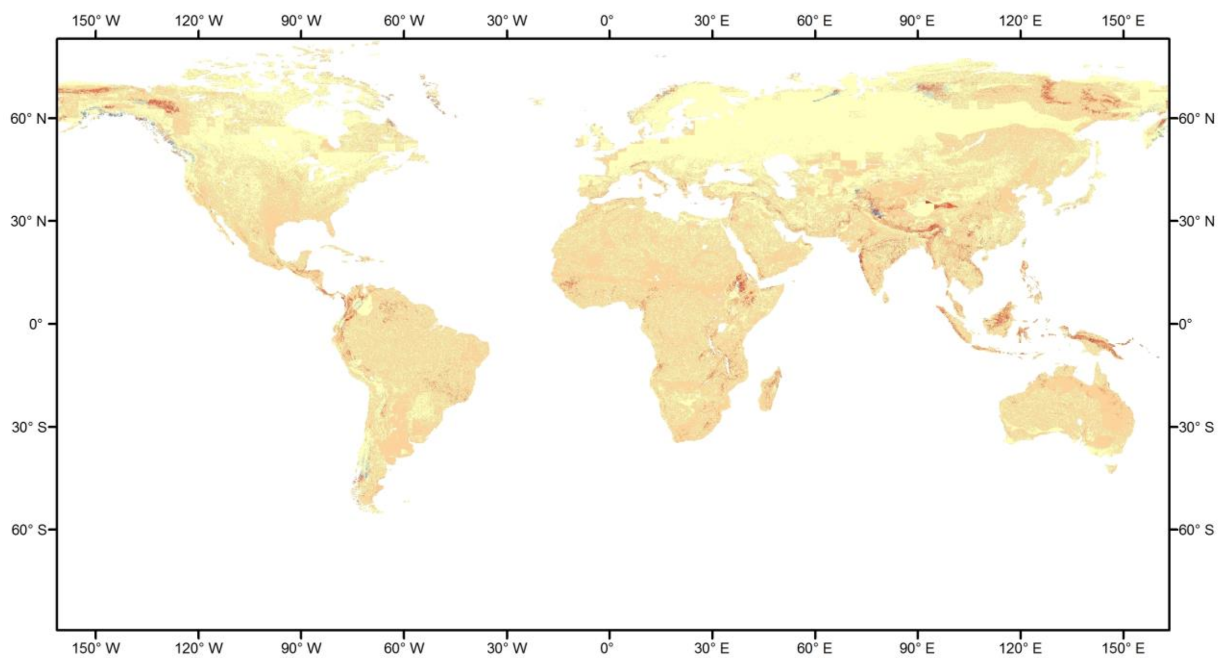

150° W
120° W
90° W
60° W
30° W
0°
30° E
60° E
90° E
120° E
150° E
60° N
30° N
0°
30° S
60° S

(C)

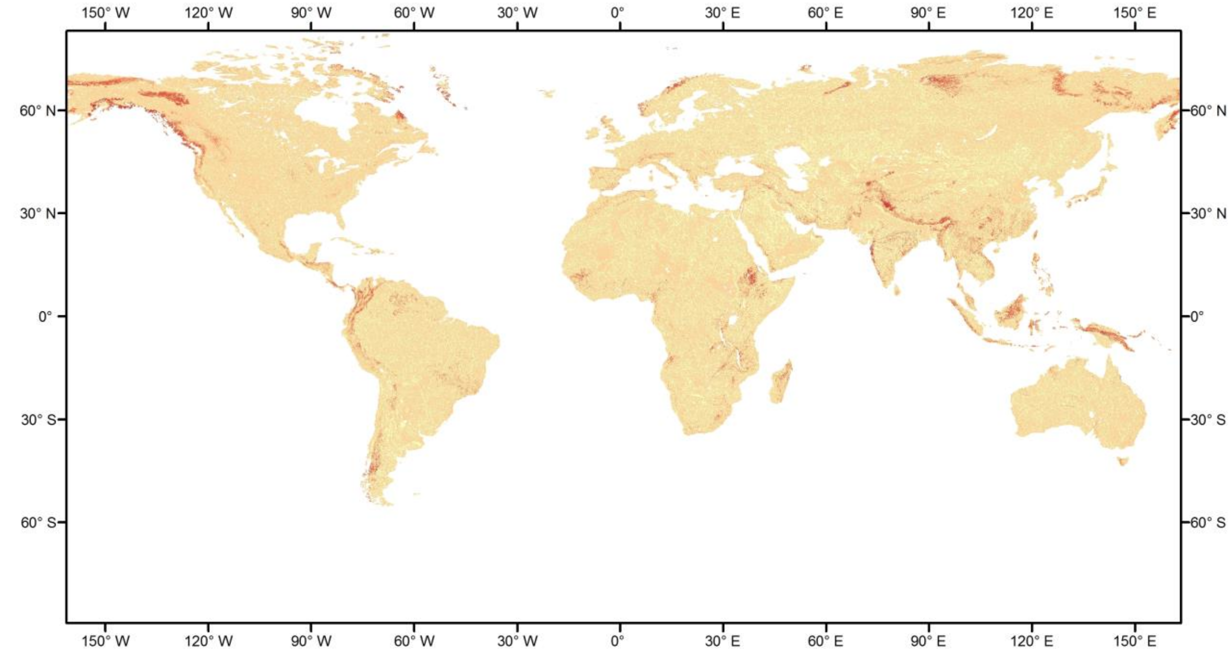
150° W
120° W
90° W
60° W
30° W
0°
30° E
60° E
90° E
120° E
150° E
60° N
30° N
0°
30° S
60° S

(D)

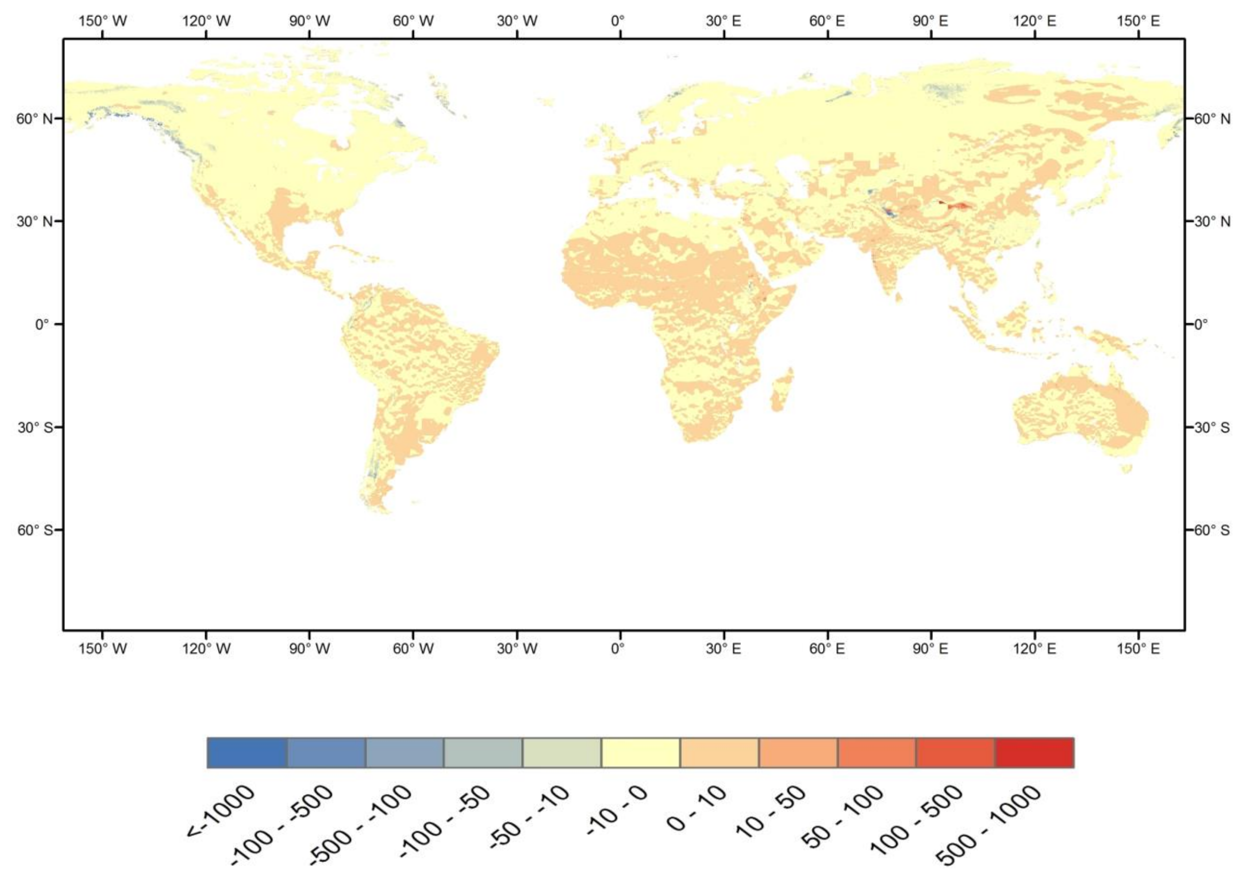
150° W
120° W
90° W
60° W
30° W
0°
30° E
60° E
90° E
120° E
150° E
60° N
30° N
0°
30° S
60° S
<-1000
-100 - -500
-500 - -100
-100 - -50
-50 - -10
-10 - 0
0 - 10
10 - 50
50 - 100
100 - 500
500 - 1000

Figure 9

(A1)

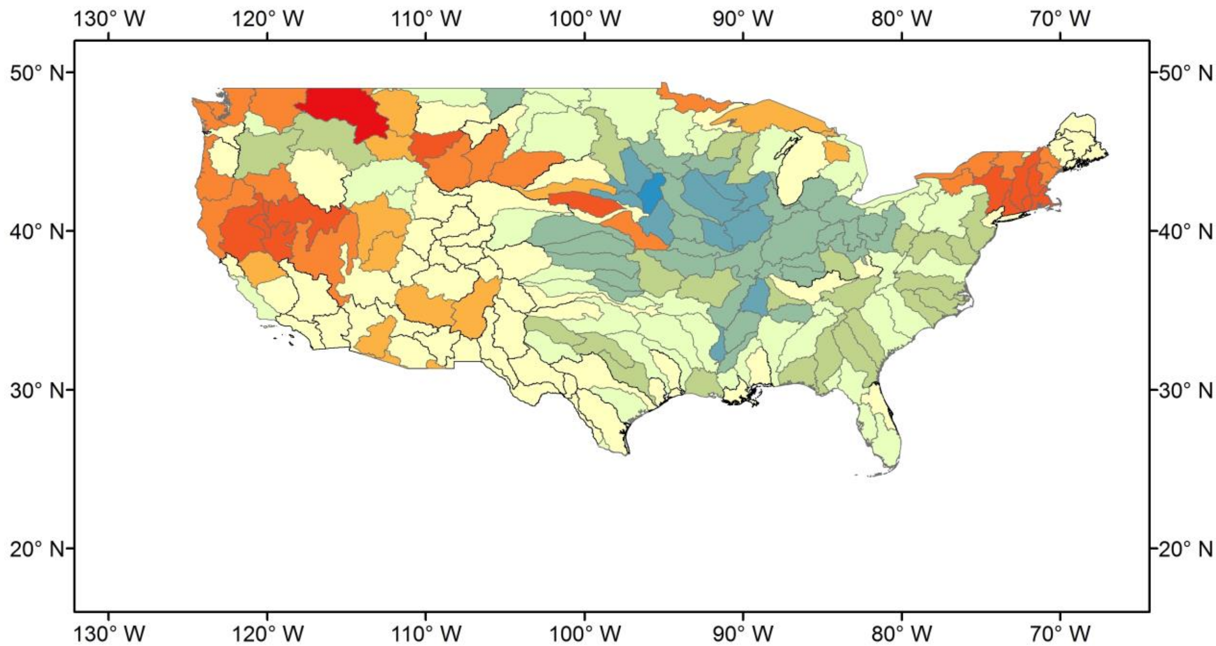

(A2)

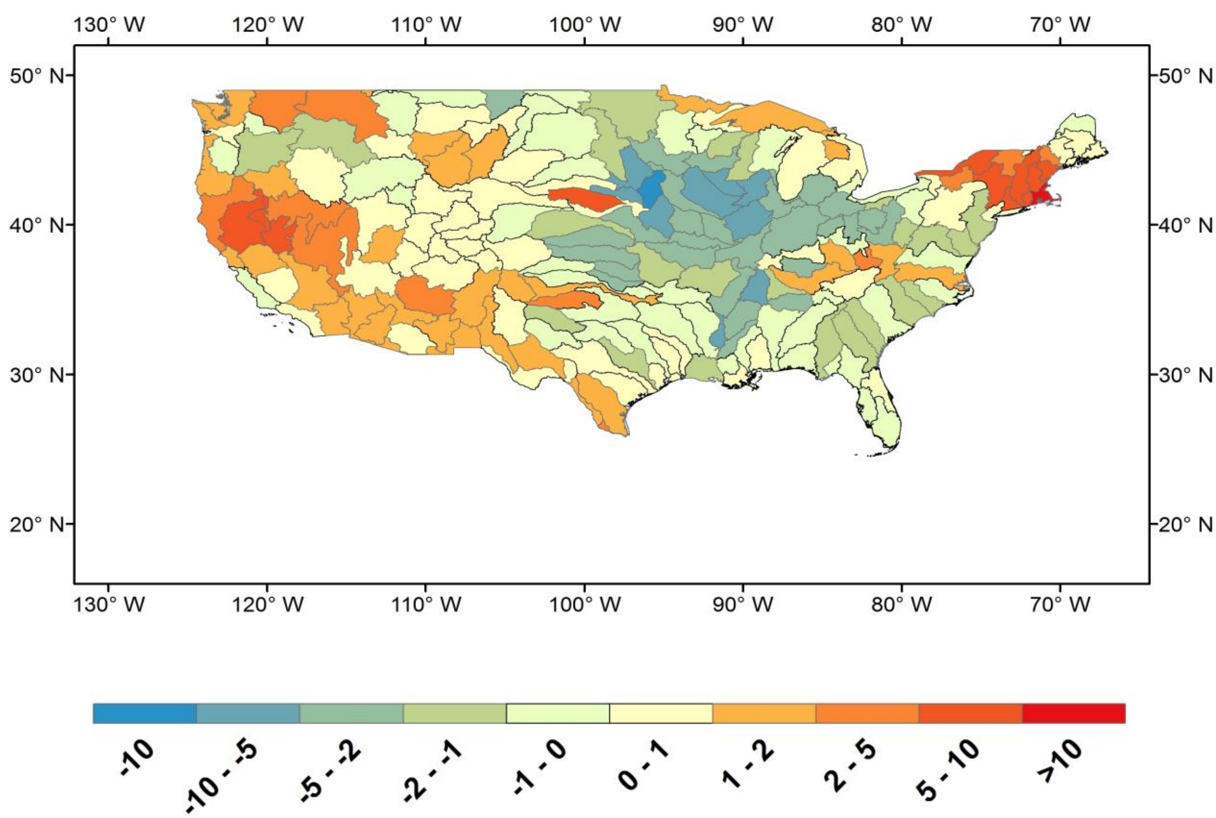

(B1)

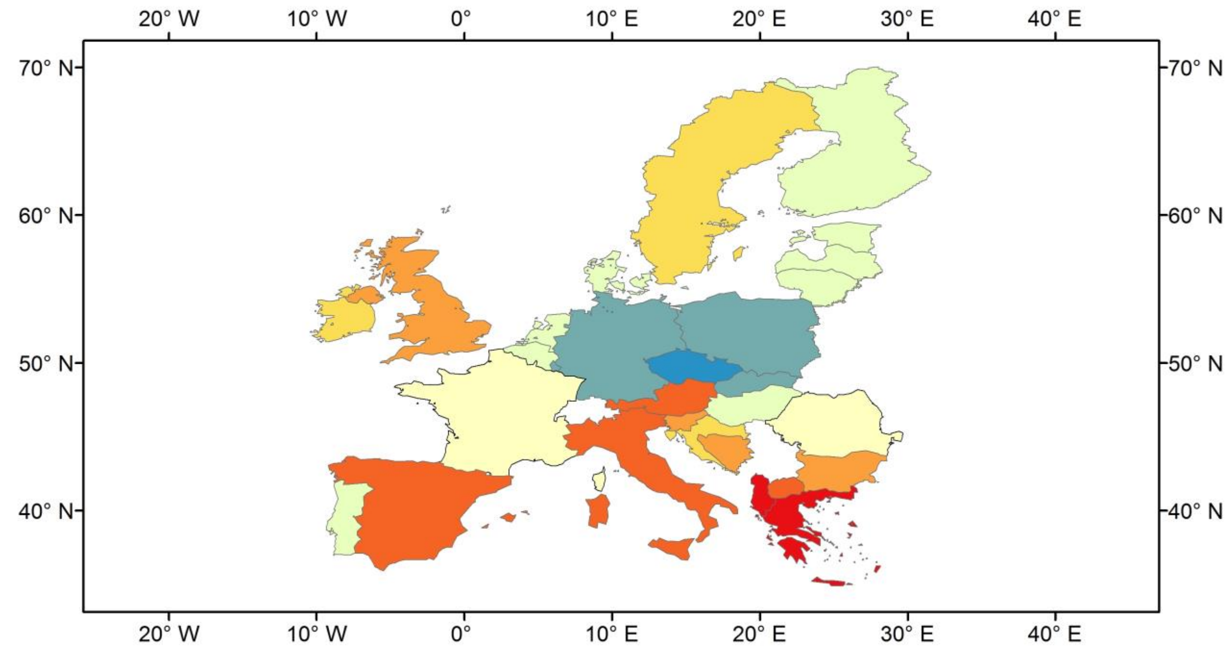
20° W
10° W
0°
10° E
20° E
30° E
40° E
70° N
60° N
50° N
40° N

(B2)

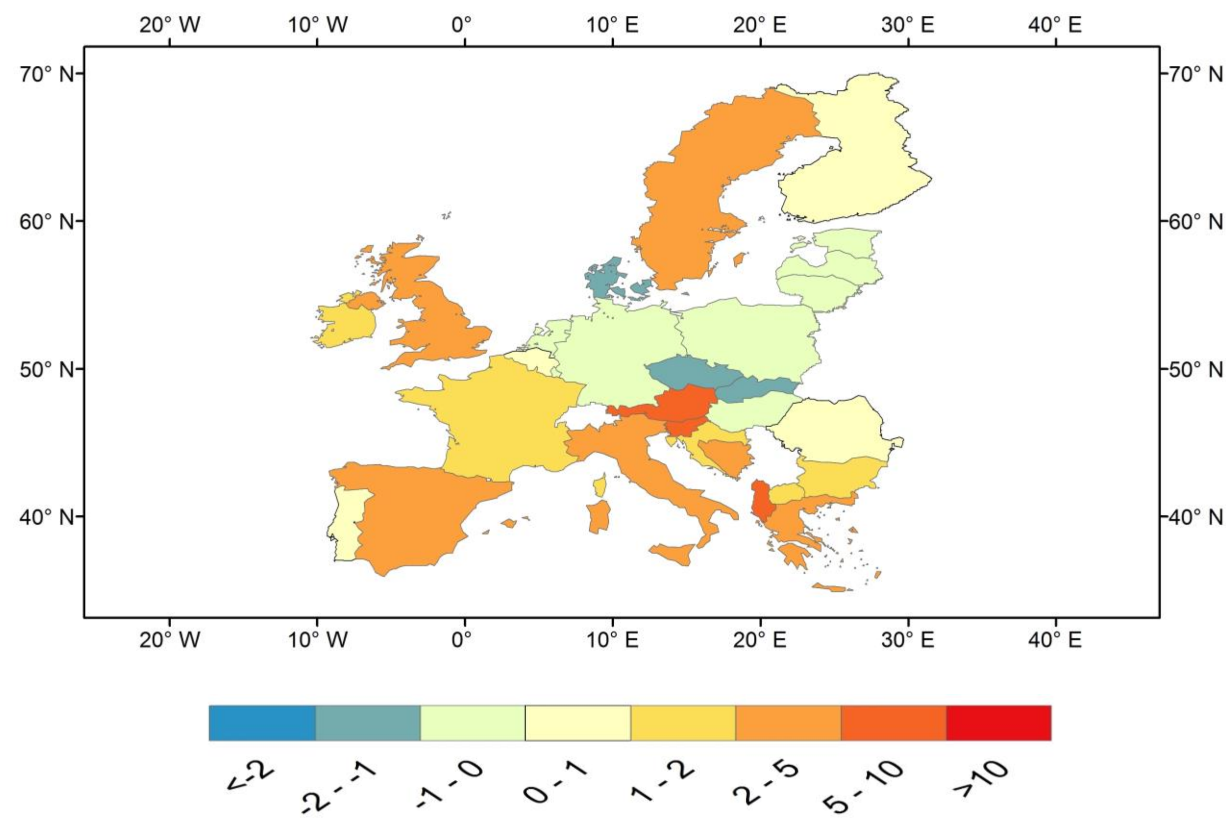
20° W
10° W
0°
10° E
20° E
30° E
40° E
70° N
60° N
50° N
40° N
<-2
-2 - -1
-1 - 0
0 - 1
1 - 2
2 - 5
5 - 10
>10